Robert Libman Zalkan

OBSERVATION OF HUGH FREQUENCY INTERNAL WAVES IN THE PACIFIC OCEAN.

UNIVERSITY OF CALIFORNIA

San Diego

Observation of High Frequency Internal Waves in the Pacific Ocean

A dissertation submitted in partial satisfaction of the requirements for the degree Doctor of Philosophy in Oceanography

by

Robert Libman Zalkan

Committee in charge:

Professor Fred N. Spiess, Chairman
Professor Charles S. Cox
Professor John D. Isaacs
Professor Walter H. Munk
Professor Richard H. Rosenblatt

1968

TABLE OF CONTENTS

LIST OF FIGURES

LIST OF TABLES

ACKNOWLEDGEMENTS

This research was carried out under the supervision of Professor Fred Spiess who was the first to foster my interest in the internal motions of the sea. His encouragement and capable guidance have been greatly appreciated. Further insight into particular aspects of the problem was gained through various discussions with Professors Charles Cox and Walter Munk.

I wish to thank Earl Squier of the Marine Physical Laboratory (MPL) for his help with the data collection system, Charles Mundy (MPL) for the construction of the array of booms, and Dave Baldwin and Dale Good of the Naval Electronics Laboratory for their help with the isotherm followers. Charles Colburn (MPL) and Larry Occhiello (MPL) were particularly helpful in collecting the data and maintaining the equipment while at sea. The many services provided by the crew of the R/P FLIP deserve a special note of appreciation.

Financial support for this study was supplied by the Office of Naval Research through a contract with the Marine Physical Laboratory, Scripps Institution of Oceanography, University of California.

Student support was provided by the Chief of Naval Personnel, U.S. Navy, through the Junior Line Officer's Advanced Scientific Educational Program (Burke Program).

VITA

February 26, 1940 - Born - Scott Field, Illinois

1961 - B.S. - United States Naval Academy, Annapolis, Maryland

1961 - U.S. Naval Submarine School

1962-1963 - U.S.S. Greenfish (SS-351)

1963 - U.S.S. Sandlance (SS-381)

1963 - 1968 - Junior Line Officer's Advanced Scientific Educational Program

1963 - University of California, Berkeley

1963 - 1968 - University of California, San Diego

1965 - M.S. - University of California, San Diego

FIELDS OF STUDY

Major Field: Oceanography

Studies in Physical Oceanography and Geophysics
Professors Robert S, Arthur, Charles S. Cox, and George E. Backus

Studies in Mathematics and Signal Processing
Professors Jacob Korevaar, Fred N. Spiess, and Richard A. Haubrich

Studies in Marine Geology and Nearshore Processes
Professors Francis P. Shepard and Douglas Inman

Studies in Biological Oceanography
Professor John A. McGowan

Studies in Chemical Oceanography
Professor Charles D. Keeling

ABSTRACT OF THE DISSERTATION

Observation of High Frequency Internal Waves

in the Pacific Ocean

by

Robert Libman Zalkan

Doctor of Philosophy in Oceanography

University of California, San Diego, 1968

Professor Fred N. Spiess, Chairman

Observations of high frequency internal waves were made from 1 to 14 December 1966, in the deep sea off Baja California. The fluctuations of the depth of an isotherm were measured with a three-element horizontal array attached to a stable platform.

The waves are characterized as a broad band

phenomenon with a continuous distribution in frequency. For short intervals of time, a narrow frequency band within the continuum is adequately described as a horizontally plane wave of a single vertical mode. Furthermore, this simplified structure is stationary over time spans of several days. High modes are present in the low frequency waves. Above 4 cycles per hour, however, the first mode predominates.

The spectral shape is consistent with the shear limited equilibrium spectrum proposed by Phillips (1966). In addition, the predominance of the first mode at high frequencies further emphasizes the importance of shear instability in internal wave propagation.

The horizontal properties of the wave field indicate well-defined directions of narrow-beamed propagation. These directions and the dispersive properties of the propagation have led to the identification of local topographic features as generating areas of internal waves.

CHAPTER I

INTRODUCTION

Since internal waves constantly change the interior structure and velocity fields of the ocean, they may have important effects on dynamic height calculations, current measurement, mixing, marine organisms, underwater sound propagation, and submarine operations. An adequate description of the wave field is required in order to determine the extent of these effects. In addition, an understanding of the mechanisms of generation and decay is necessary to the determination of the role internal waves play in energy transfer processes. Specifically, the description should include modal structure, energy spectra, and directional information.

At the present level of theoretical development, a model that adequately describes these features is clearly not feasible, and little is known about the mechanisms of generation and decay. Our purpose, therefore, is to seek such a description from observation of high frequency internal waves in the deep sea.

The complex structure of internal waves makes both data collection and analysis difficult. Unlike surface waves, internal waves do not have a unique dispersion relationship. Instead, there is a different relationship

for each member of the infinite set of possible modes. In addition, the maximum vertical displacements of these waves occur at intermediate depths rather than at the free surface, and are, therefore, difficult to observe.

To overcome these difficulties, simultaneous measurements of the fluctuating depth of an isotherm were recorded with a three-element horizontal array. This procedure allows the establishment of a phase difference (travel time) relationship leading to a vector wave number and, therefore, directional determination. The wave number magnitudes can then be tested against the theoretical dispersion curves for confirmation of progressive wave phenomena.

Stokes (1847) first showed that internal waves can exist in a stratified fluid consisting of two homogeneous layers. Later Webb (1884) and Greenhill (1887) dealt with the multi-layered case. In 1933, Fjeldstad extended the theory to include a continuous density gradient. More recent systematic treatments of the subject are by Eckart (1960) and Tolstoy (1963). A summary of the theory of small amplitude internal waves in still water is given in Appendix A.

Several investigators have attempted to obtain directional information by towing a thermistor chain in a sequence of traverses of different direction. This procedure allows one to obtain a directional description of the wave field by interpretation of measured Doppler shifts.

Using this method, Metcalf et al (1962) reported internal waves of 17 minute periods traveling south from the equator. However, LaFond (1964) in the Pacific and Charnock (1965) in the Atlantic, had little success.

Ufford (1947) appears to be the first to make simultaneous measurements of internal waves at spatially separated points. His first method was to make repeated lowerings of bathythermographs from the bow, midsection, and stern, of a ship located over the San Diego trough, in 1200 meters of water. The results were inconclusive, due to the small phase differences and, therefore, large error limits in the determination of wave number. To increase the phase differences, Ufford moved to shallow water (40 meters) and employed both bathythermograph lowerings from three anchored ships and a buoyed array of three thermocouples. Unfortunately, each observation spanned only a few hours of time, and he used only those portions of the records (average 1 hour, 7 minutes) in which a single frequency predominated.

Further work in shallow water (18 meters) has been accomplished at the Navy Electronics Laboratory's Oceanographic Tower. Here, a three-element array of isotherm followers has been successfully used to determine directional information (LaFond 1962a, Cox 1962). Nevertheless, mid-oceanic observations are still required since shallow water propagation differs considerably from that in

deep water. In particular, the wave form,and therefore the frequency content, is affected by the nearness of the sea floor (LaFond, 1961b) and the propagation direction by shoreward refraction (LaFond,1962b). Also, there is probably a preference for the first mode at all frequencies, since the shallow depth, and thus narrow waveguide, means large shear for modes greater than one.

We, therefore, seek our information from the deep ocean. The difficulty of employing the array technique in deep water is attested to by the previous absence of such measurements.

CHAPTER II

OBSERVATIONAL EQUIPMENT

A three element horizontal array was obtained by attaching heavy duty booms to the Research Platform FLIP's (Fisher & Spiess, 1963) bow or upper structure. The attachment was done by hinges enabling the booms to be properly stowed while FLIP was in the horizontal position. Cables to the sea-sensing units were fed over the ends of the booms. Upon "flipping" to the vertical position, the booms were rigged out to form an equilateral triangle of 30.5 meters (100 feet) per side (Figure 1). Each boom had its own independent sensing system consisting of 1) an isotherm follower, 2) a vertical staff of four variable frequency thermometers, and 3) a vibrotron pressure guage.

The isotherm follower is controlled by a thermistor in a sensing unit. A servo system is arranged to vary the depth of the sensing unit in such a way that the temperature measured by the thermistor remains constant. The thermistor signal is developed across a DC bridge. One leg of the bridge is connected by a cable to a thermistor in the sea-sensing element. The other leg is composed of a variable bank of resistors for selection of the desired temperature. When the thermistor has the same resistance as the variable resistors, the bridge is in balance. When the temperature

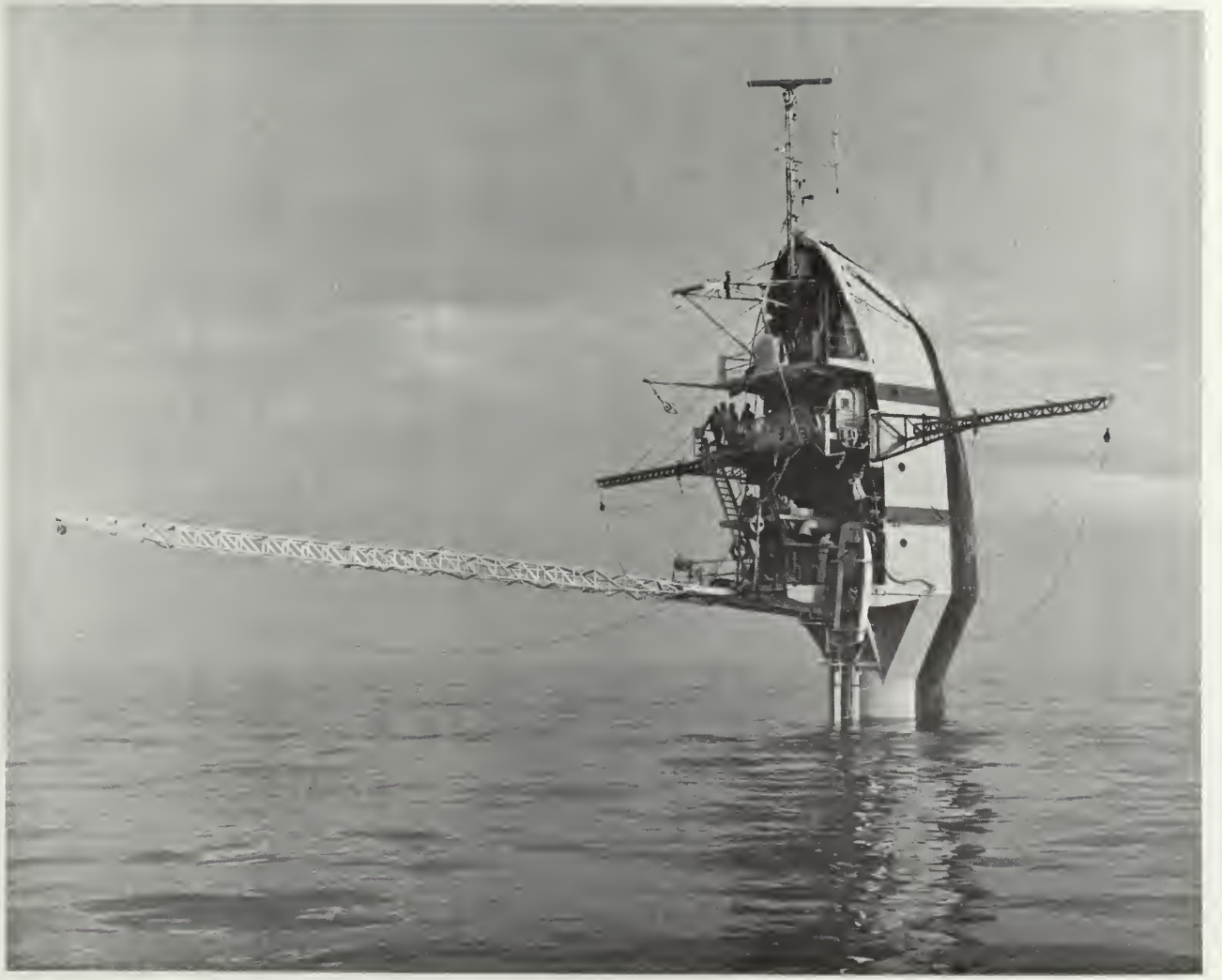

Figure 1. Triangular array attached to the Research Platform FLIP.

at the thermistor changes, the thermistor changes resistance and a DC voltage occurs across the bridge. This voltage is fed through magnetic amplifiers and silicon controlled rectifiers to the windings of a DC motor. The polarity and amplitude of the signal determine the direction and speed at which the motor turns. The motor drives a winch which raises or lowers the sea-sensing element until the bridge is again in balance. In this way the thermistor in the sea-sensing unit is kept at the depth of an isotherm and hence the name Isotherm Follower (LaFond, 1961a; Good, 1968).

The upper part of the sea-sensing element is a hollow pressure case. A vibrotron pressure guage was installed in this portion and exposed to sea pressure via an oil-filled chamber with a flexible diaphragm. The output of the vibrotron was used for determining the depth of the sea-sensing unit.

Since servo-systems are subject to dead bands (i.e., a certain level of signal is necessary before the system responds), a staff with four variable frequency thermometers (Squier, 1967) was installed on each sea-sensing unit to be used as a vernier. The thermometers were placed .6 meters (2 feet) and 1.8 meters (6 feet) above and below the servo-system thermistor. A scheme of interpolation was then used to determine the actual depth of the isotherm (see Appendix B).

The data were recorded both digitally for later

analysis and by analog methods for on the spot monitoring. The digital data collecting system consisted of 1) a clock, 2) a sequential sampling unit, 3) a counting system, and 4) an incremental tape recorder. Every twenty seconds the clock put out a pulse which triggered the sampling unit. The sampling unit consisted of a stepping switch which sequentially connected each of the channels of information to the counting system for one second's duration. The counting system was a period counter set to determine the number of microseconds required for 4096 cycles of signal. This number, along with a serial time count, was then recorded on magnetic tape by an incremental recorder. The information recorded from each of the sea-sensing units consisted of the vibrotron pressure signal, the four variable frequency thermometer temperatures, and the vibrotron pressure signal again. Each follower was sampled in turn and then the azimuthal orientation of the array was recorded to conclude the cycle. After the 19 pieces of information had been recorded, there was one second of dead time. Then the clock sent out a pulse and the whole procedure started again.

DC voltages for analog recording were obtained by sending the three vibrotron signals and one temperature signal to frequency meters. The output voltage from the meters drove the pen displacement system of a four channel chart recorder.

Since FLIP is free to rotate about the vertical

axis, it was necessary to employ an azimuthal orientation system. An error signal between the desired heading and FLIP's actual heading and a rate of rotation signal from the gyrocompass repeater were used to drive the tilt boxes of two hydraulic motors. The motors in turn drove two off-axis propellers. The torque from the propellers would rotate FLIP until the desired heading was achieved. If FLIP drifted off the desired heading the system would again be activated to maintain the desired heading.

A block diagram of the data collection and orientation systems is shown in Figure 2.

Preliminary data were obtained during February, March, and April of 1966 while Flip was operating in Hawaiian waters. Analysis of these data indicated the need to:

1. increase the sensitivity and reliability of the isotherm followers
2. incorporate the thermometer staffs as verniers
3. change the data recording system to incorporate 2
4. reposition the booms and winches
5. change the cable fairleads because of 4
6. replace lightweight telescoping booms with heavy-duty ones
7. employ the orientation system to keep the array stabilized in azimuth for as long a time as possible.

The implementation of these modifications resulted

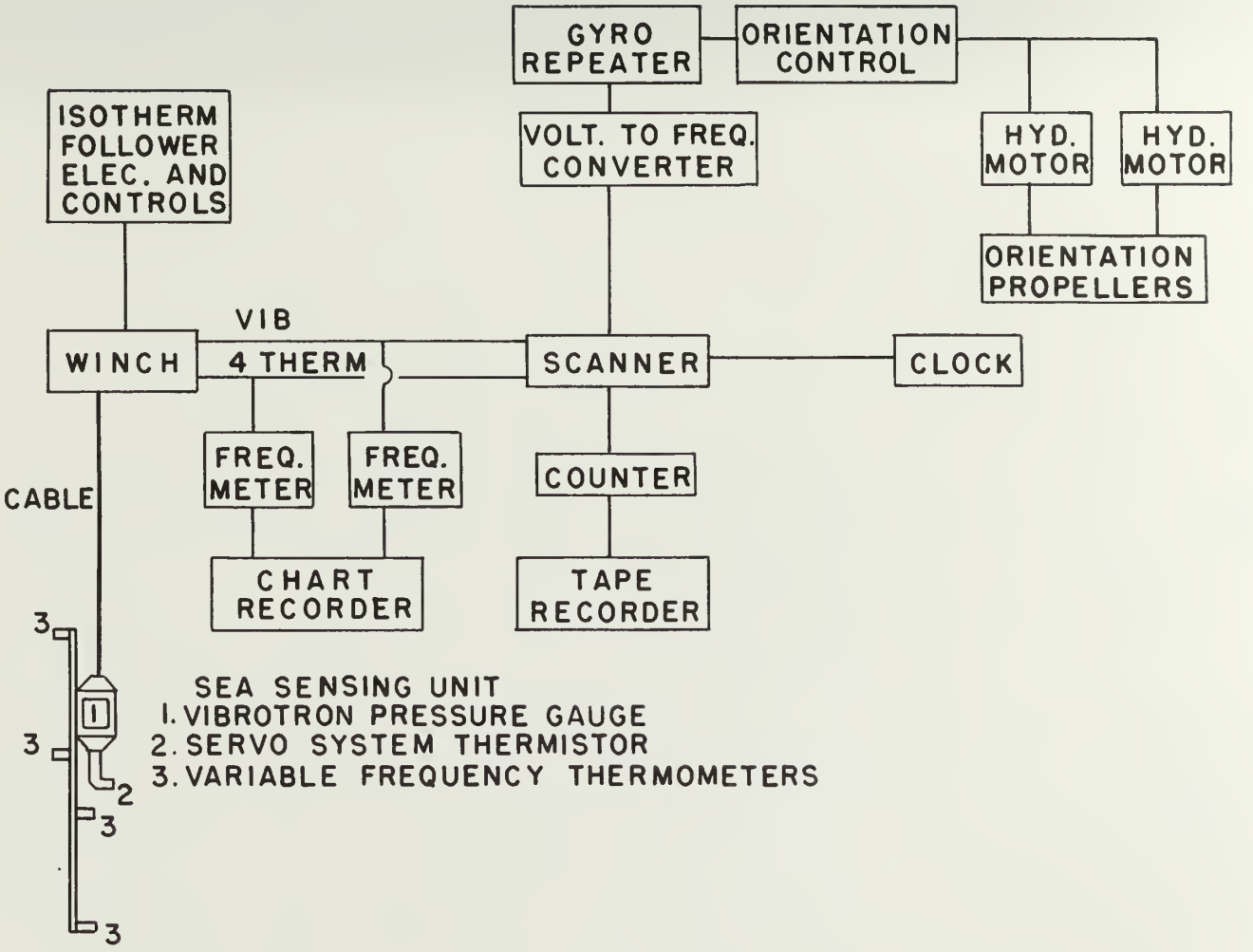

Figure 2. Block diagram of data collection and orientation systems.

in the system described above. A short seatrial was conducted near Catalina Island in November. Then FLIP was towed to deep water off Baja California and data were collected during December 1966.

CHAPTER III

OBSERVATIONS

A station southwest of San Diego (near 30°N,121°W) was maintained from 1 December 1966 to 14 December 1966. FLIP was allowed to drift with the mean integrated current over her 300 foot draft. Since the waves travel relative to the current, this drift minimized any Doppler effects. A track of FLIP's drift is shown in Figure 3.

Due to the aerodynamic characteristics of FLIP's upper structure, she tends to orient with her keel into the wind. Once she has self-oriented, the propeller system has little trouble maintaining the heading. If the wind direction shifts more than twenty degrees, however, the load becomes too great on the propeller system and re-orientation is required. It was possible, nevertheless, to break the data into 15 short series during which the variance of array orientation was small. The duration, mean azimuth of the keel, and azimuthal standard deviation are given in Table I.

Time records of series 4, 5, and 6 are presented in Figure 4, and are typical examples of the internal oscillations during the entire sampling period. Each series contains isotherm depth vs. time from all three followers. The middle trace corresponds to the depth scale on the left.

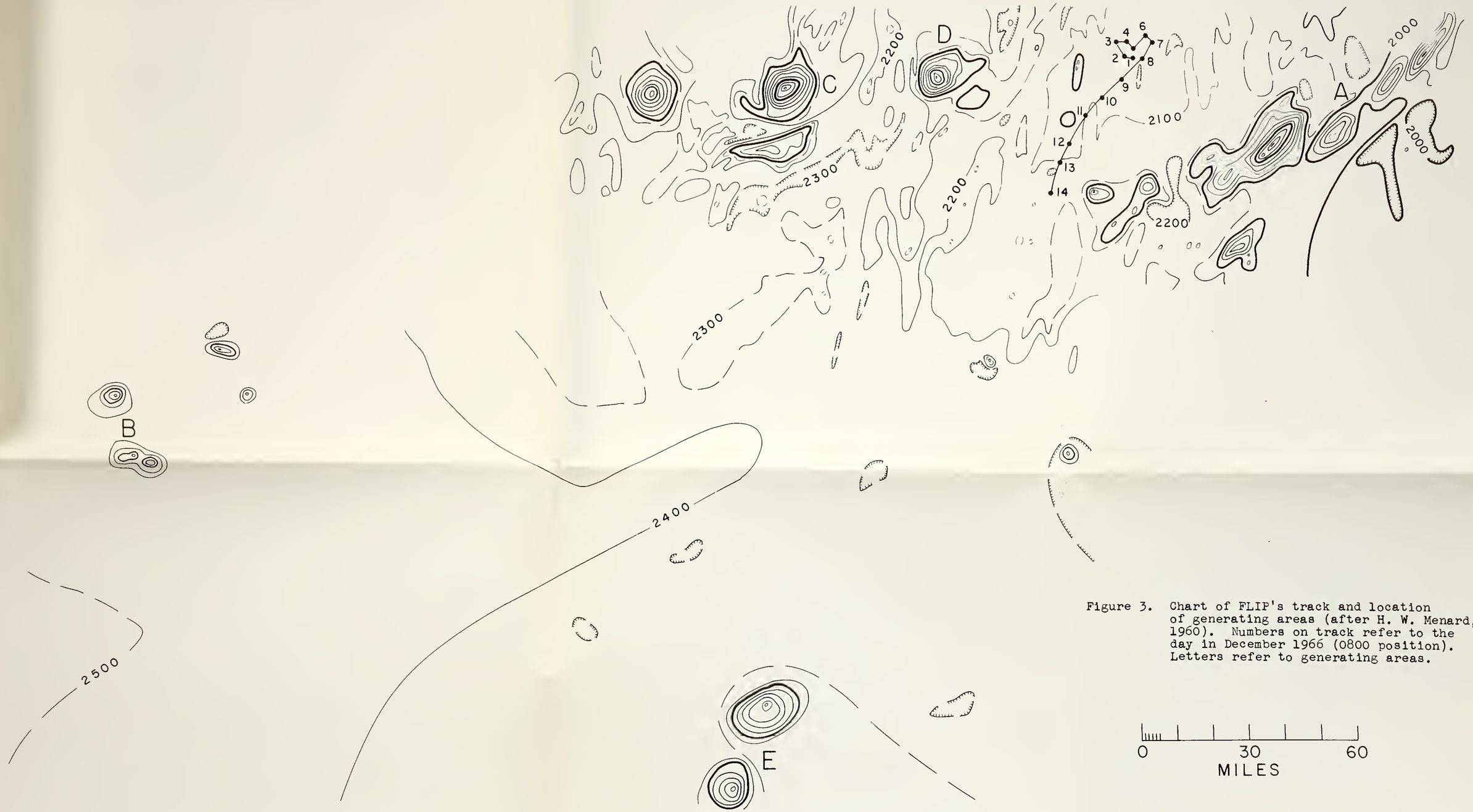

Figure 3. Chart of FLIP's track and location of generating areas (after H. W. Menard, 1960). Numbers on track refer to the day in December 1966 (0800 position). Letters refer to generating areas.

TABLE I

Division of Data into 15 Series

SERIES NO.	TIME (Dec. 1966)	MEAN HEADING (^{o}T)	STANDARD DEVIATION(^{o}T)
1	061400-021120	329.2	4.8
2	021120-031005	239.8	3.2
3	021827-031712	240.2	3.1
4	031816-041701	240.7	2.6
5	041701-051547	240.6	1.2
6	051819-061704	239.1	2.8
7	070115-071633	348.5	2.7
8	071633-080625	328.5	4.1
9	080751-090636	343.2	4.3
10	090636-100515	342.4	1.9
11	100557-110443	011.8	2.3
12	101430-111315	010.4	3.5
13	120338-122108	002.4	27.3
14	122108-132003	356.5	6.8
15	132003-140556	007.6	10.6

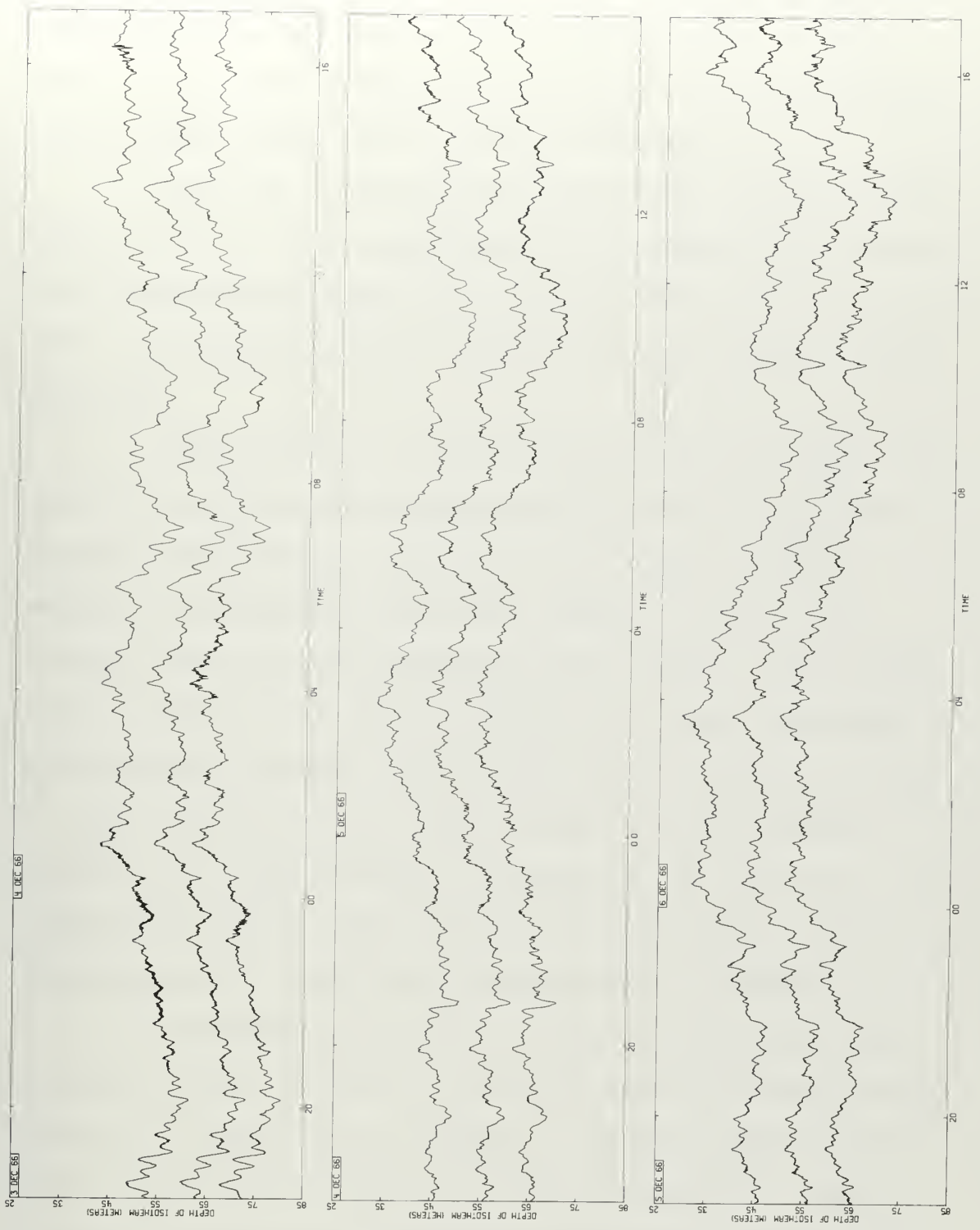

Figure 4. Depth of the observed isotherm vs time.
The upper and lower traces have been offset ∓ 10 meters.

The upper and lower traces have been offset $\pm$ 10 meters respectively. The interpolation scheme used to calculate the isotherm depth may be found in Appendix B.

The first characteristic one should notice in the time records is the predominance of the tidal oscillations. Tidal frequencies contain most of the energy and are, therefore, responsible for the largest vertical motions of the isotherm.

Superimposed on the tidal motions are the high frequency fluctuations with which this thesis is concerned. Several interesting properties of the high frequency motions are apparent in the time records. First, the records from the three elements exhibit good visual coherence throughout the data. Second, the larger amplitudes of the high frequency oscillations seem to come and go as if they were modulated. And finally, the oscillations appear to be always present, indicating, at least in a qualitative manner, that they may be stationary. These conclusions are justified quantitatively in Chapter V.

The second property, i.e. that of amplitude modulation, has been observed in shallow water by LaFond (1961) and may be caused by two effects. The most likely cause of this amplitude fluctuation is the beating effect. When energy is present as a continuous spectrum, beating occurs among the various frequencies and a rapidly varying amplitude envelope is developed.

The second possible cause is a resonance condition described by Eckart (1961) and hereafter referred to as Eckart Resonance. When the waves are propagated in a well-localized group -- localized in space, frequency, and wave-number -- a resonant coupling between the layers of high stability can occur. The effect of this resonance is to cause the energy to oscillate between the layers. If the conditions are variable along the propagation path, and one measures the motion in one layer only, an amplitude modulation will be observed, with the modulating frequency dependent upon the sharpness of the layers and their vertical separation. The same effect would be observed if the source is not stationary in a spatial sense. That the necessary conditions for this resonance existed is shown in Chapter IV.

CHAPTER IV

ANALYSIS TECHNIQUES

The power spectrum has become a basic tool for presenting the properties of long complicated time series in a condensed form. Here, the method of first Fourier transforming and then summing over the squares has been employed.

Consider a discretely-sampled, real series of finite length, X(j), j = 0, N - 1. The X(j) may be represented by the complex series

$$X(j) = \sum_{m=0}^{N-1} \hat{X}(m)\, e^{i2\pi jm/N}, \quad j = 0, N-1 \tag{1}$$

Then the complex Fourier coefficients are:

$$\hat{X}(m) = \frac{1}{N} \sum_{j=0}^{N-1} X(j)\, e^{i2\pi jm/N}, \quad m = 0, N-1 \tag{2}$$

Taking into account the symmetry of the transform of a real series, a spectral estimate of elementary frequency bands with two degrees of freedom is obtained by

$$S_x(m) = A_m\, \hat{X}(m)\, \hat{X}^*(m), \quad m = 0, \frac{N}{2} - 1 \tag{3}$$

where * denotes complex conjunction and $A_m = 1$, $m=0$

$Am. = 2$, $m>0$

To increase spectral stability, a sum over adjacent elementary bands is formed.

$$S_x(h_c) = \sum_{m=p}^{q} S_x(m) = \sum A_m \hat{X}^*(m)\ \hat{X}(m) \qquad (4)$$

where p and q are the lower and upper band indices over which it is desired to sum and $h_{center} = \frac{p+q}{2}$. Letting $a = q - p + 1$ (the number of bands included in the sum), equation (4) yields 2a degrees of freedom per estimate. Since it is desirable to model a continuous spectrum of infinite extent which has dimension length^2 /cycle/time = L^2T, it is necessary to divide S(h) by the band width, a. Thus

$$E_x(h_c) = \frac{S_x(h)}{a} = \frac{1}{a} \sum_{m=p}^{q} A_m \hat{X}^*(m)\ \hat{X}(m) \qquad (5)$$

and simple summing is replaced by band averaging.

The conversion from the indices m, h_c, a, to frequency is accomplished by using the sampling interval Δt.

Let $N\Delta t = T$

then $\frac{2\pi jm}{N} = 2\pi(j\Delta t)\frac{m}{T}$

so that $f = \frac{m}{T}$, $f_{center} = \frac{h_c}{T}$, and $\Delta f = \frac{a}{T}$

A further discussion of these techniques is presented by Tukey in Harris (1966). Haubrich (1965) shows that these methods produce the same result as those of transforming the correlation function. The actual calculations were performed on a CDC 3600 digital computer using

the fast Fourier transform techniques of Cooley and Tukey (1965).

Once the series has been transformed, the cross spectral estimate between two series is simply

$$G_{xy}(h_c) = \frac{1}{a} \sum_{m=p}^{q} A_m \hat{X}^*(m)\, \hat{Y}(m) \tag{6}$$

The estimates of coherence and phase difference are respectively:

$$R^2_{xy}(h_c) = \frac{\left|G_{xy}(h_c)\right|^2}{E_x(h_c) E_y(h_c)} \tag{7}$$

and

$$\phi_{xy}(h_c) = \mathrm{Arg}\,(G_{xy}(h_c)),\ y \text{ leads } x \tag{8}$$

Considering the triangular array 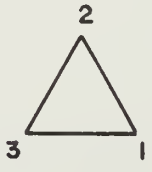

$$\sum_{l} \phi_l(h_c) = \sum_{l} \mathrm{Arg}(G_l(h_c)),\ l = 12, 23, 31 \tag{9}$$

For a single train of plane waves, equation (7) is identically equal to 1 , and equation (9) is identically equal to 0. Loss of coherence and a non-zero $\sum \phi_l$ may be caused by a finite beam width (Munk et al, 1963; Cox, 1962).

Cox also discusses reduction of coherence caused by turbulence and variable phase velocity. It should be noted that if a = 1 (i.e. p = q) equation (7) has only one degree of freedom and $R_\ell(h_c)$ is constrained to be equal to one. Similarly, $\sum \phi_\ell(h_c)$ in equation (9) is constrained to be equal to zero. Therefore it is necessary to band average. Failure to average over at least two bands would lead to the conclusion of plane wave propagation, when some other form of propagation may exist.

Using the three phase differences defined in equation (8), it is possible to determine three vector wave numbers. Let vector wave number k have components (k_x, k_y). The three phase differences, ϕ_ℓ for plane wave propagation become

$$\phi_\ell = k_x X_\ell + k_y Y_\ell \tag{10}$$

where X_ℓ and Y_ℓ are the spatial separation components between elements of the array. Since there are three equations and only two unknowns, (k_x, k_y), the wave number is over determined. Considering the equations two at a time, three separate solutions for the vector components may be found.

Then

$$k_{rms} = \left[\frac{1}{3}\sum_{m=1}^{3} \left|k_m\right|^2\right]^{1/2} \tag{11}$$

where

$$k_m = ik_x + jk_y \qquad m = 1,3 \tag{12}$$

i and j being unit vectors in the x and y directions and m indexing the three sets of solutions.

The mean direction of propagation is defined as

$$\theta = \mathrm{Arg}\,(\vec{k}_1 + \vec{k}_2 + \vec{k}_3) \tag{13}$$

Beam width indication, $\Delta\theta$, is defined as

$$\Delta\theta = \left|\max(\mathrm{Arg}(\vec{k}_i)) - \min(\mathrm{Arg}(\vec{k}_j))\right| \quad i,j=1,3\,;\, i\neq j \tag{14}$$

where the branch cut is taken to form $\Delta\theta$ as the minimum angle between vector solutions k_1 and k_j (as in figure 5).

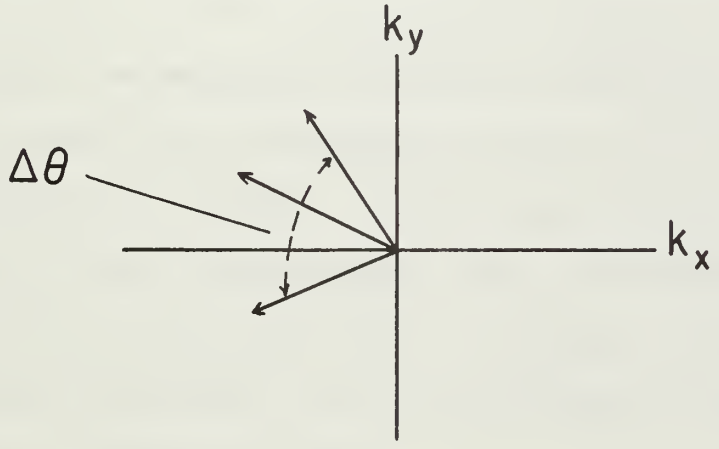

Figure 5

Definition of $\Delta\theta$

It should be noted that if $R_\ell = 1$ and, thus, $\sum\phi_\ell = 0$, then only two of the equations are independent, the k_m's are identical, and $\Delta\theta = 0$. These results agree with the earlier discussion of plane wave propagation.

Once a vector wave number with a small $\Delta\theta$ has been found, it becomes necessary to determine whether the motion is due to internal waves or to some other mechanism such as anisotropic turbulence. The distinction between wave motion and motions due to other causes can be made with the help of diagnostic dispersion curves. The solutions, k_{rms}, are, plotted on an $\omega - k$ diagram and tested against the theoretical dispersion curves to see if there is agreement. It must be remembered, however, that solutions which fail the test may still be wave motions not due to single plane waves (i.e. multiple modes, or two or more plane waves of the same mode and frequency traveling in different directions, etc.).

To obtain the dispersion curves, it is first necessary to calculate density, ρ (z), from the observed temperature, T(z), and salinity, S(z), distributions. Next $\rho(z)$ is used to calculate $N(z)$. Finally, for each frequency band of interest, the wave equation is numerically integrated to solve for the k_n.

Figures 6 and 7 show the observed temperature and salinity distributions, the calculated density and stability frequency distributions, and the theoretical dispersion curves for the first 10 modes. Figure 6 reflects conditions just prior to the commencement of wave data collection, and Figure 7 reflects the conditions immediately after terminating data collection. The temperature distribution in the upper 200 m was obtained by manually lowering an isotherm

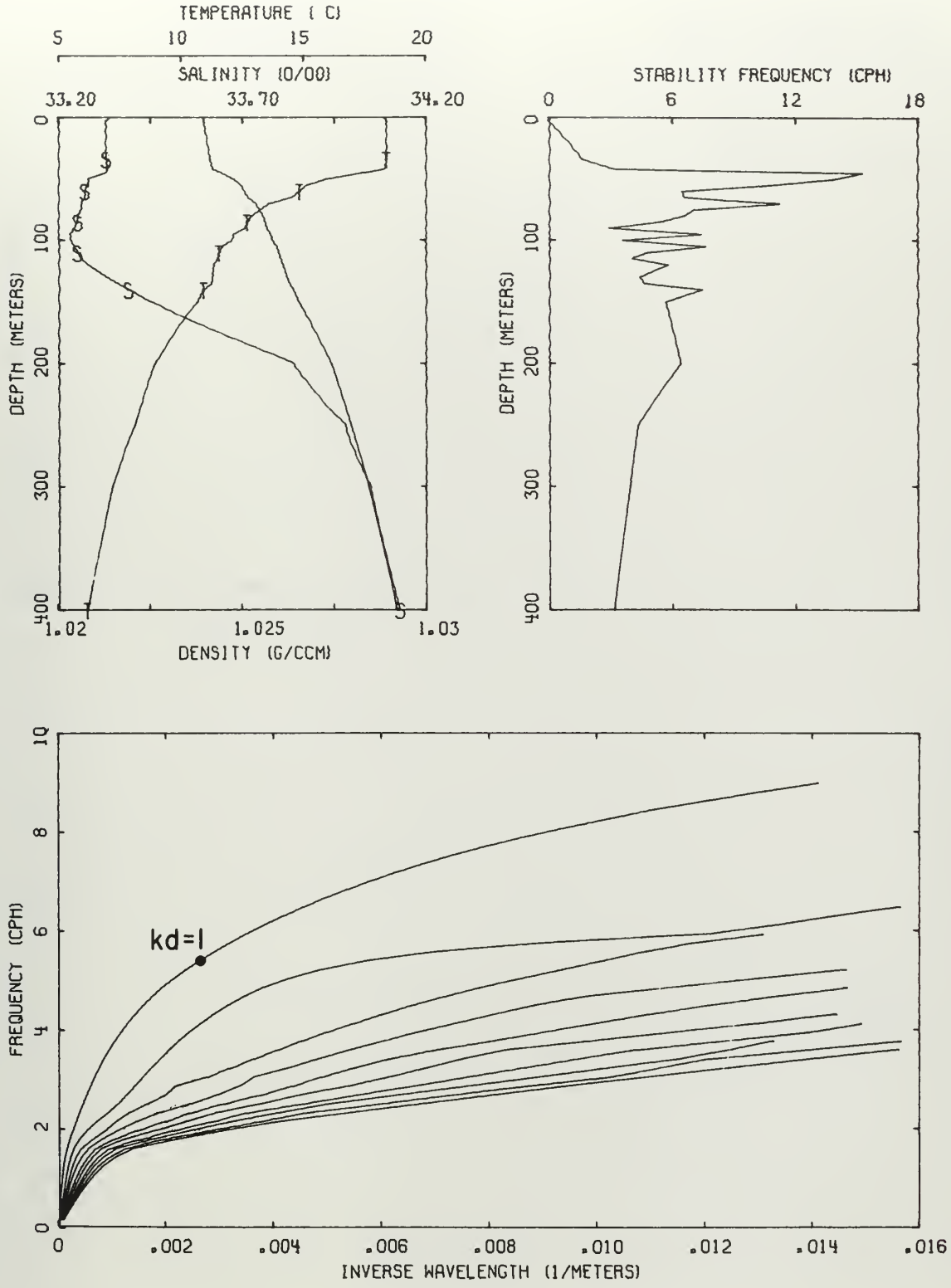

Figure 6. Propagation conditions for 1 December 1966.

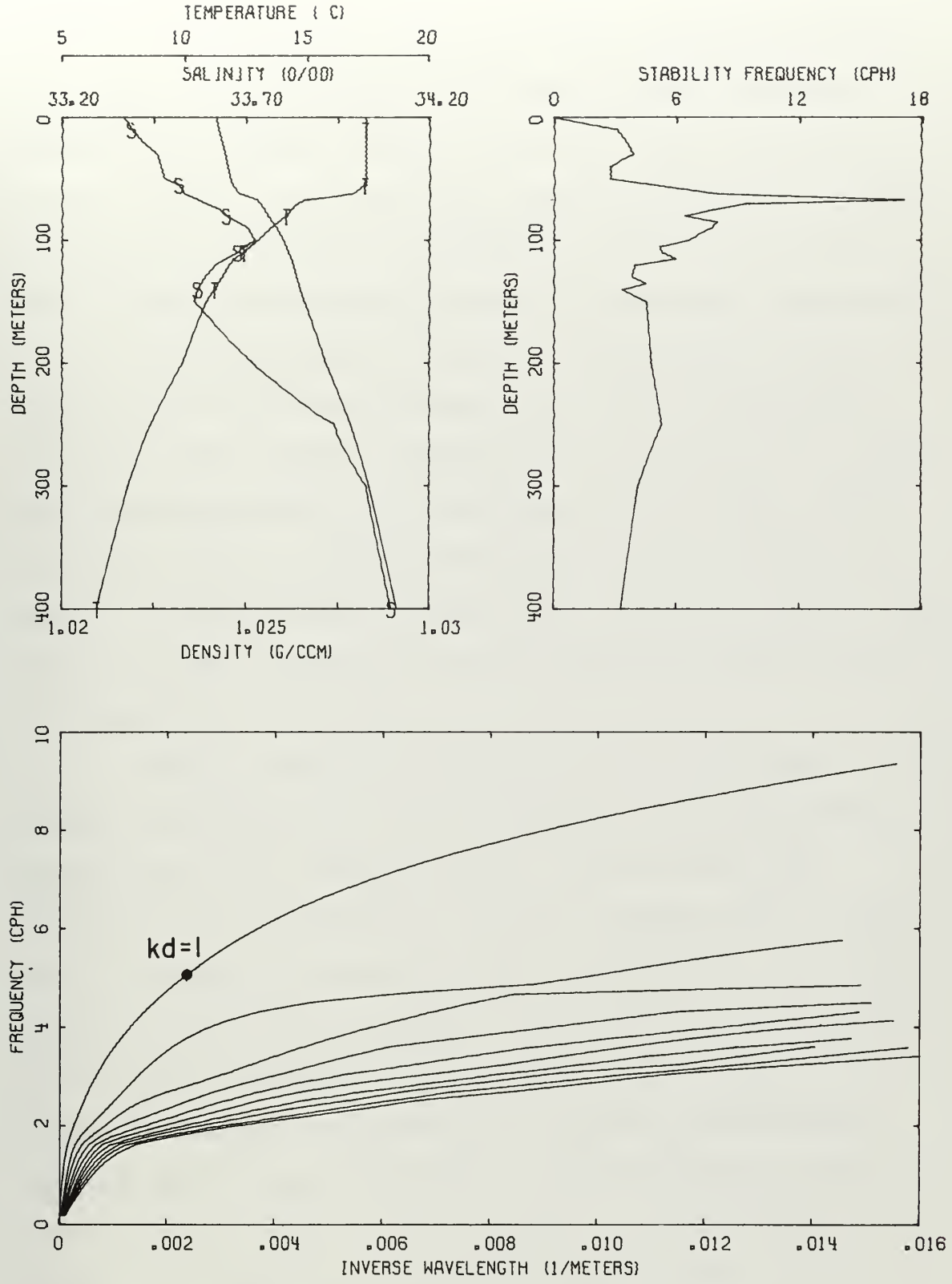

Figure 7. Propagation conditions for 14 December 1966.

follower. The distributions of salinity and of temperature below 200 m were obtained from nearby CalCOFI stations (Figure 6 in December, Figure 7 in May). The difference in the two salinity distributions at shallow depths is probably attributable to sampling at different seasons as opposed to being a permanent spatial feature. In any case, temperature is the controlling factor within the thermocline and the salinity distributions were used for "order of magnitude" purposes. Since spatial aliasing will occur for $\lambda^{-1} > .016$, the dispersion curves are terminated at this value. Below 400 meters T(z) and N(z) monotonically decrease while S(z) and ρ (z) monotonically increase with increasing depth. The values of these parameters corresponding to figures 6 and 7 are tabulated in Table II.

Several features of Figures 6 and 7 are worth further consideration. Both stability frequency distributions have many relative maxima. These maxima are reflected in the dispersion curves as wiggles (Fig. 6, 3rd. mode) or changes in curvature (Fig 6, 2nd mode). It is the coupling between these layers of high stability which produces Eckart Resonance. The greater the vertical separation between the layers, the sharper the resonance. The resonance regions are shown in the dispersion curves as areas where two modal lines converge and then diverge. For example, in Figure 7, a resonance region between the second and third mode is apparent at a frequency slightly greater

than 4cph ($\lambda^{-1} \cong .0085$). The coupling seems to occur between the layers centered about 75 meters and 250 meters. Other regions of resonance are also present.

TABLE II

Distribution of Temperature, Salinity, Density, and Stability Frequency below 400.

1 December 1966

Depth	Temperature	Salinity	Density	Stability Frequency (cph)
500	5.93	34.20	1.02993	2.88
1000	3.91	34.47	1.03320	2.28
1500	2.76	34.57	1.03622	2.06
2000	2.10	34.63	1.03912	1.93
3000	1.63	34.66	1.04472	1.77
4000	1.56	34.66	1.05021	1.76

14 December 1966

500	5.92	34.22	1.02990	3.00
1000	3.96	34.49	1.03321	2.28
1500	2.89	34.58	1.03622	2.06
2000	2.12	34.64	1.03913	1.93
3000	1.65	34.68	1.04474	1.80
4000	1.58	34.69	1.05024	1.77

The two sets of stability frequency and dispersion curves show several interesting differences. The upper high stability layer is sharper and slightly deeper in Figure 7 relative to figure 6. On the other hand, the lower layer is weaker and much deeper, increasing the separation between layers and causing the 2nd - 3rd mode resonant region to shift to a lower frequency and inverse wavenumber. While the first modal curve shifted only

slightly and only in the low frequency region, all of the higher modal curves shifted toward lower frequencies. The weakening of the intermediate relative maxima may also explain why the curves of Figure 7 are much smoother than those of Figure 6. Notice, however, that the regions of slightly negative curvature still remain in modes 2 and 3.

These differences may have been caused by both temporal and spatial changes in the internal structure. But, because the internal waves are continually changing the subsurface structure, it is possible that the mean conditions were stationary throughout the data collection interval, and that the differences between figures 6 and 7 were caused by taking the two profiles when different phase relationships existed among the waves. In this case these figures would represent perturbations about the mean conditions at the two spatially and temporally separated points.

Figure 8 shows the mean depth of the 16.85°C isotherm for series 1-12 and the 16.00°C isotherm for series 13-15 at each of the three sea-sensing elements. The 16.85°C isotherm shows large oscillations during the first 12 series. For the last three series, however, it was necessary to shift to a lower temperature in order to remain within the thermocline. Therefore, it is probable that the differences are due to a combination of both mechanisms.

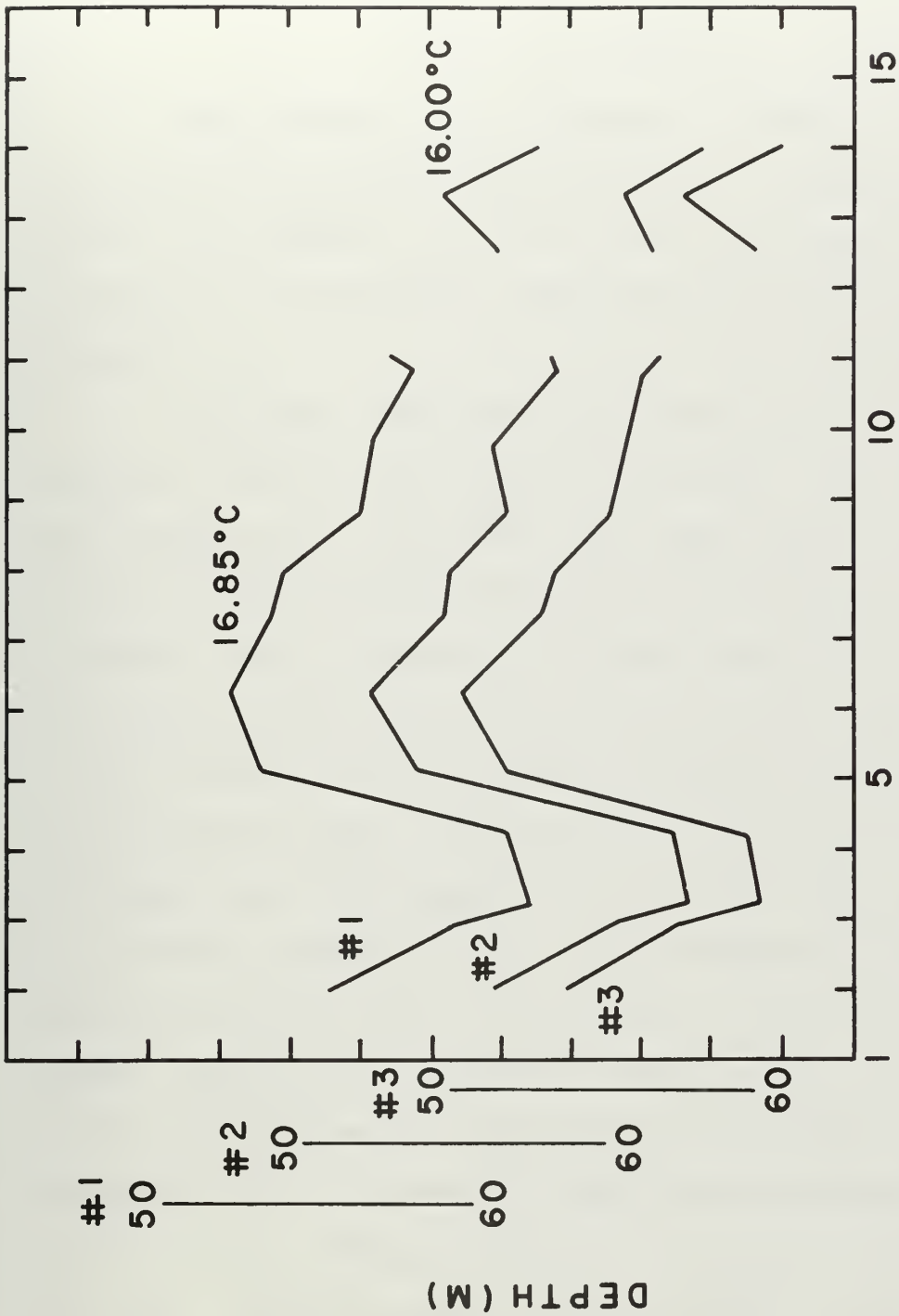

Figure 8. Mean depth of the observed isotherm vs time.

CHAPTER V

RESULTS OF ANALYSIS

The fifteen series tabulated in Table I were analyzed by the methods of Chapter IV. As examples, the results for series 1, 4, 8, 10, and 14 are shown graphically in Figures 10 through 14. The layout of each figure is as follows:

The upper left hand graph shows the three energy spectra - one for each isotherm follower. Spectral averaging (equation (5)) was done over eight elementary frequency bands yielding 16 degrees of freedom per spectral estimate. For 16 degrees of freedom, there is 80% confidence that $.58\sigma^2 < S^2 < 1.47\sigma^2$ and 95% confidence that $.43\sigma^2 < S^2 < 1.80\sigma^2$ where S^2 is the spectral estimate and σ^2 is the true spectral value. Continuing down the left hand side of the page, the second graph shows the three pair coherences as defined in equation (7). For 16 degrees of freedom, the 95% significance level for coherence is .25. The third graphs display $\sum \phi$ as defined in equation (9). The upper right hand graph shows the computed wave number magnitudes (equation (11)) plotted as points and the theoretical dispersion curves (modes 1 to 10) of 1 December 1966 plotted as lines. Since the modal lines converge in the lower frequency region, an expanded scale plot for series 1 is shown

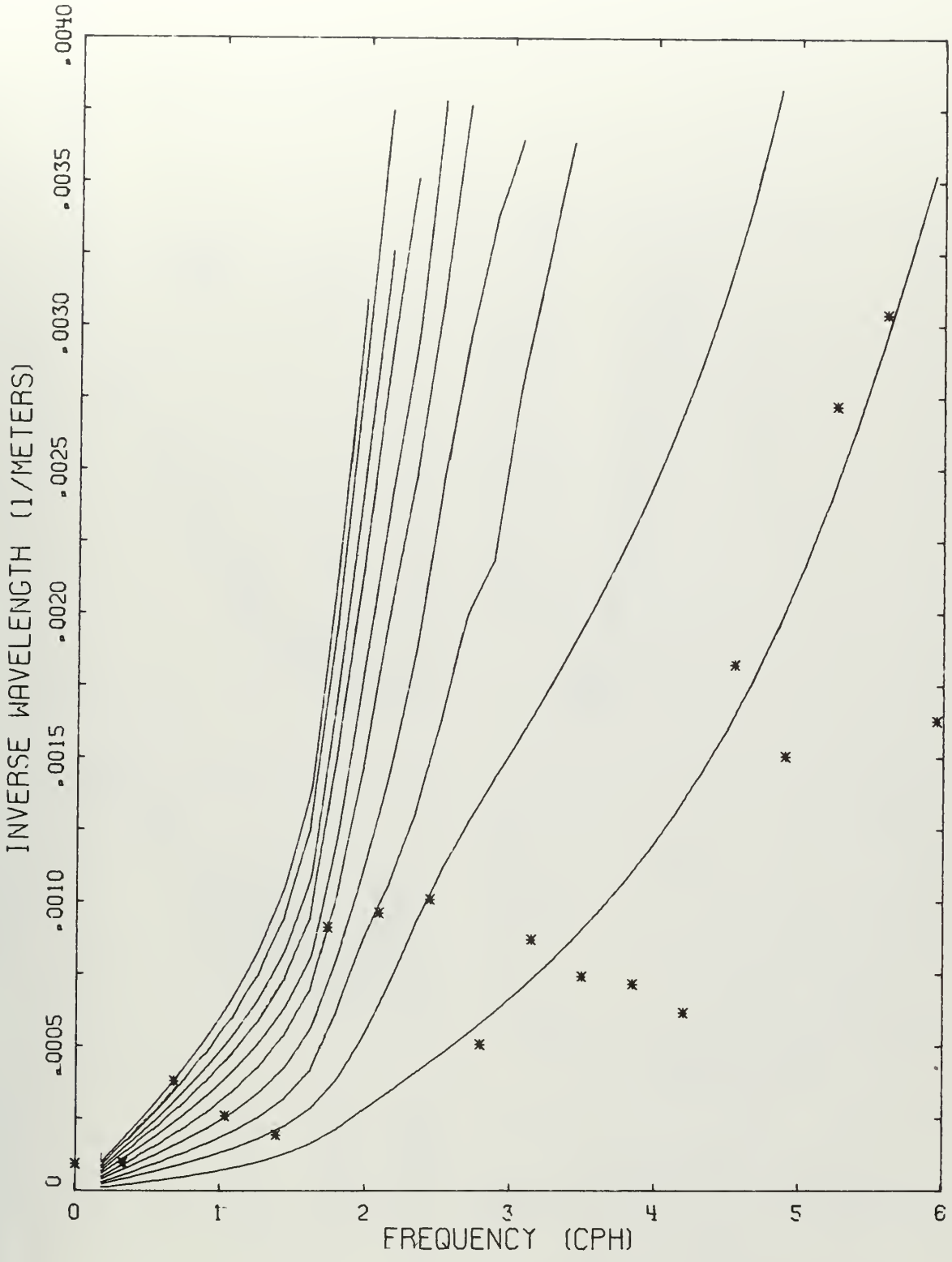

Figure 9. Expanded scale dispersion diagram for series 1.

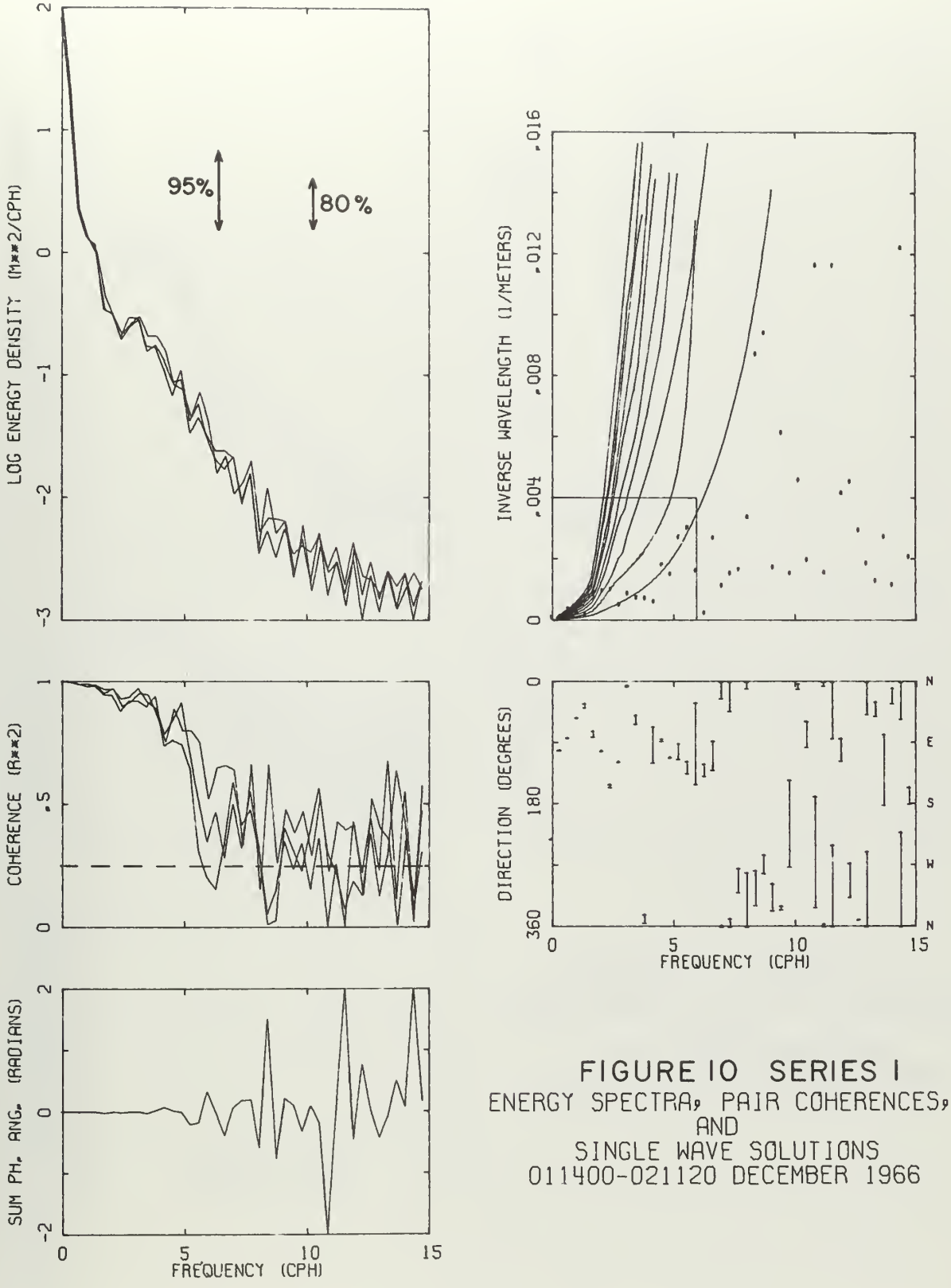

FIGURE 10 SERIES I
ENERGY SPECTRA, PAIR COHERENCES,
AND
SINGLE WAVE SOLUTIONS
011400-021120 DECEMBER 1966

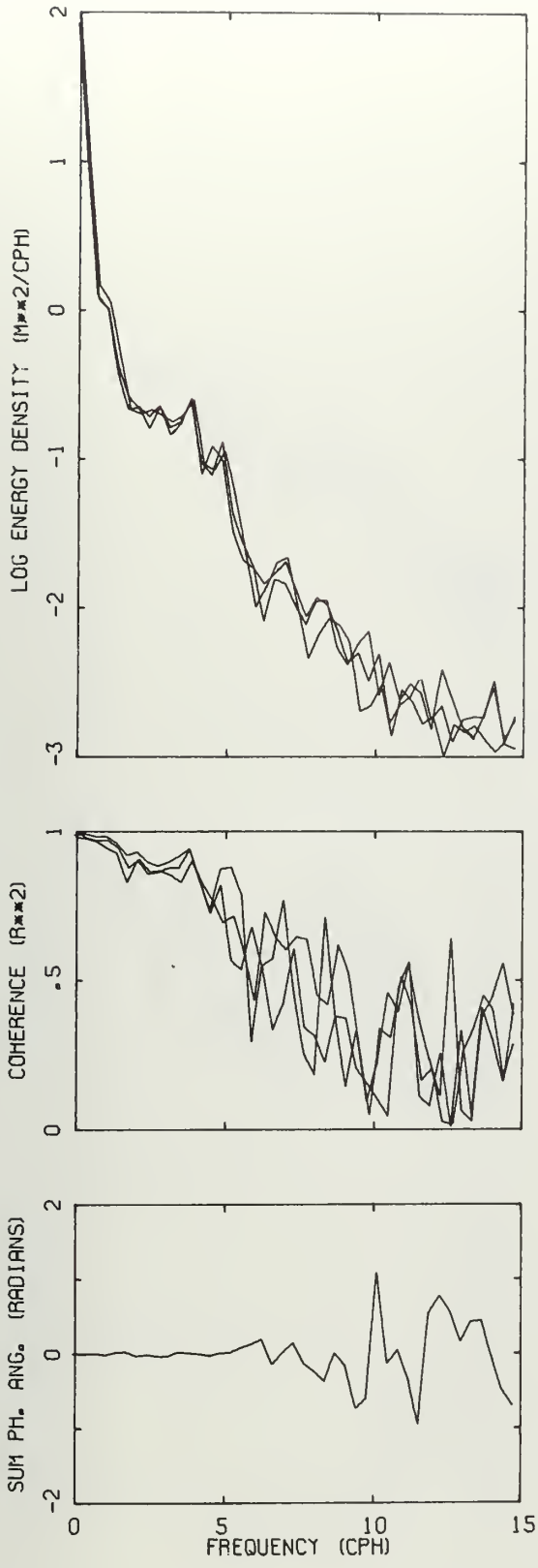

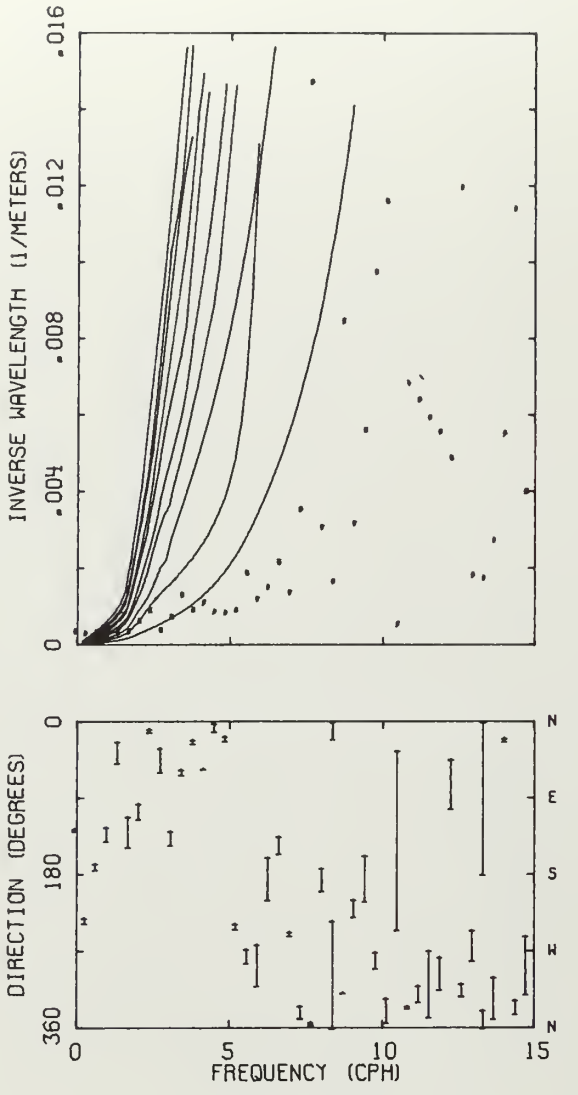

FIGURE II SERIES 4
ENERGY SPECTRA, PAIR COHERENCES,
AND
SINGLE WAVE SOLUTIONS
031816-041701 DECEMBER 1966

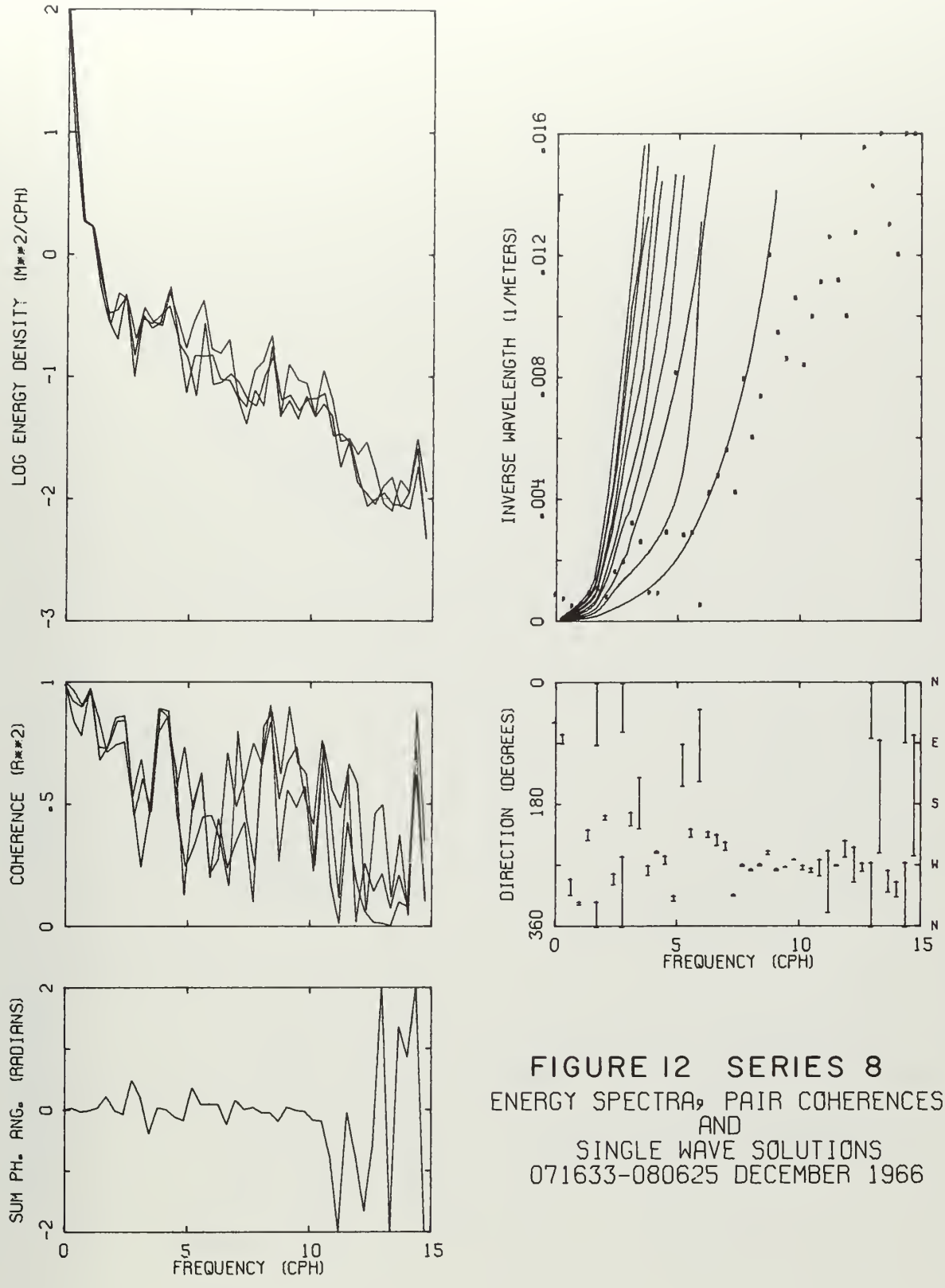

FIGURE 12 SERIES 8
ENERGY SPECTRA, PAIR COHERENCES,
AND
SINGLE WAVE SOLUTIONS
071633-080625 DECEMBER 1966

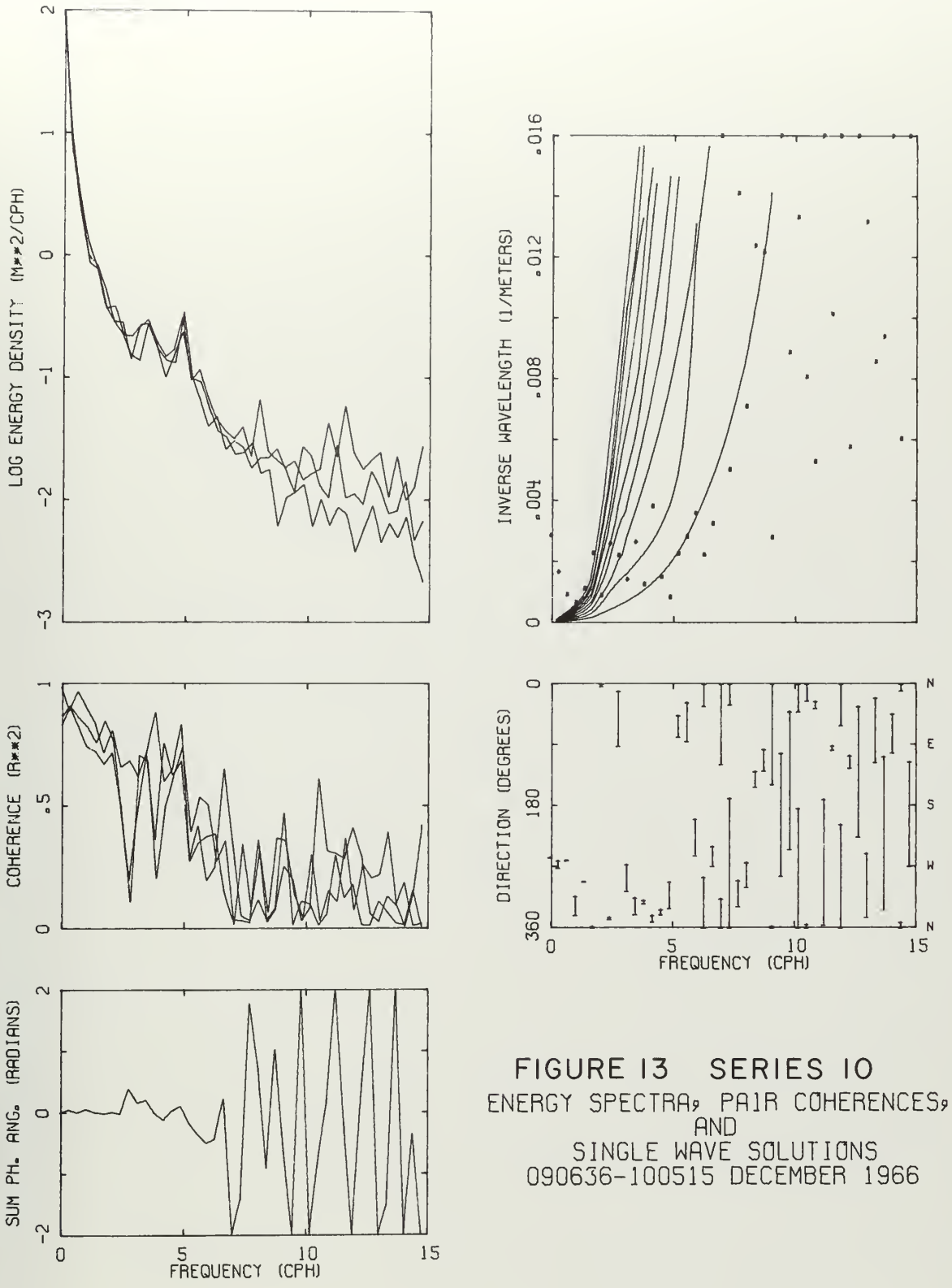

FIGURE 13 SERIES 10
ENERGY SPECTRA, PAIR COHERENCES,
AND
SINGLE WAVE SOLUTIONS
090636-100515 DECEMBER 1966

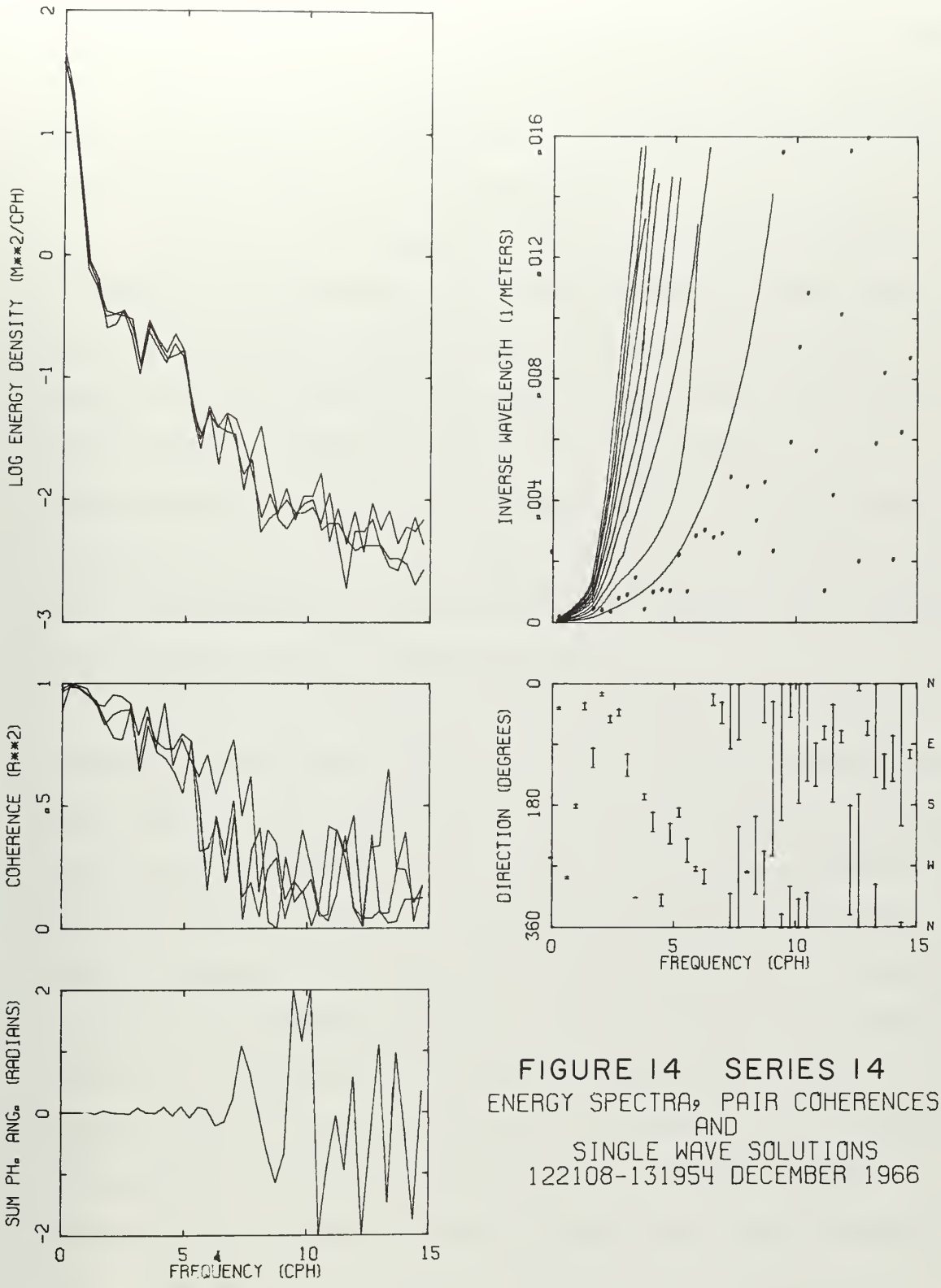

FIGURE 14 SERIES 14
ENERGY SPECTRA, PAIR COHERENCES,
AND
SINGLE WAVE SOLUTIONS
122108-131954 DECEMBER 1966

in Figure 9 (corresponds to boxed area of figure 10). The final graph displays the directional information. Each line runs from $(\theta-\frac{\Delta\theta}{2})$ to $(\theta+\frac{\Delta\theta}{2})$ where θ and $\Delta\theta$ are defined by equations (13) and (14) respectively.

Various narrow band spectral peaks are apparent throughout the 15 series. However, the peak heights lie between the 80% and 95% confidence limits and the frequencies at which they occur change from series to series. The peaks are caused by nearby frequencies having the proper phase relationships to accentuate their particular frequency band during the short duration of sampling. This result is consistent with the expected results from sampling a continuous, random, Gaussian process.

The coherence is quite high for the lower frequencies but in some cases falls off quite rapidly in the 5 to 7 cph region. Similarly, $\sum \phi$ remains close to zero when the coherence is high and then appears to oscillate randomly as the coherence drops. The rate at which the coherence falls is greatest when the energy spectrum is also falling rapidly with frequency and vice versa. A possible explanation for the fall off is that in these cases there appears to be a lack of first mode solutions at the higher frequencies. For modes greater than 1, the wavelength becomes smaller than the array spacing near these frequencies. Therefore as frequency increases more and more wavelengths occur between the elements of the array (see

Cox 1962). In other cases, however, the coherence rises again to quite high values and then falls off in the 10 cph region with $\sum \phi$ behaving in a consistent manner. In these cases, there appears to be a predominance of first mode solutions above 5 cph (compare series 1 and 8).

Some of these solutions, particularly above 5 cph, lie to the right of the first mode dispersion curve but have good coherence, small $\sum \phi$, and narrow beam width, $\Delta\theta$. In several series, these solutions actually seem to form a separate modal line below that of the first mode. The best example can be found in series 8 where there is a multitude of narrow beamed high frequency waves traveling toward 270°. The most likely cause of this phenomenon is a Doppler shift due to current shear. FLIP drifts with the mean integrated current over her entire 300 foot draft and these high frequency waves are superimposed on the mean integrated current over their relatively narrow high stability layer (see Figures 6 and 7). The difference between these currents required to account for the observed Doppler shifts is on the order of only 5 cm/sec. The details of the necessary calculations and a specific example may be found in Appendix C.

The solutions considered acceptable as single wave propagation, together with their modal numbers and mean propagation directions are listed in Table III. Solutions falling below mode 1 are included as mode 1 and those

TABLE III

Summary of Acceptable Solutions

FREQUENCY SERIES		Band No. 2	3	4	5	6	7	8	9	10	11	12	13	14	15	16	17	18	19	20	21	22	23	24	25	26	27	28	29	30	31	32	33	34	35	36	37
		CPH .33	.68	1.03	1.38	1.74	2.09	2.44	2.79	3.14	3.49	3.84	4.20	4.55	4.90	5.25	5.60	5.96	6.31	6.66	7.01	7.36	7.71	8.06	8.42	8.77	9.12	9.47	9.82	10.17	10.52	10.88	11.23	11.58	11.93	12.28	12.63
1	Mode	5	10	4	2	5	3	2	1	1	1	1	1	1	1	1	1			1					1	1		1									
	Direction	101	082	053	035	077	102	153	118	006	055	348	093	086	112	102	126			108					303	268		332									
2	Mode	10	4	4	2	8	2	2	1	1	1	1	1	1	1	1	1	1	1	1	1	1															
	Direction	194	281	312	021	165	047	152	128	028	111	010	083	115	347	136	075	178	138	150	128	157															
3	Mode	8	3	3	1	5	1	2	1	1	1	1	1	1	1	1	1	1	1	1	1	1	1	1	1	1	1		1	1							
	Direction	340	307	233	039	075	085	154	148	224	038	078	052	089	131	138	132	192	161	127	136	165	231	215	168	254	221		235	220							
4	Mode	10	9	5	3	2	2	2	1	1	1	1	1	1	1	1	1	1	1	1	1	1	1	1		1		1	1	1							
	Direction	233	170	132	036	130	105	010	045	137	059	023	055	006	020	240	275	286	184	145	249	341	354	185		318		184	280	339							
5	Mode	10	4	5	2	2	3	2	2	1	1	1	1	1	1	1	1	1	1	1	1	1	1	1		1	1	1									
	Direction	141	210	095	094	110	114	352	122	069	062	295	121	309	334	315	185	170	166	247	251	276	263	290		285	286	278									
6	Mode	5	3	3	9	3	3	1	2	1	1	1	1	1		1	1	1	1	1	1	1	1	1		1				1							
	Direction	225	046	194	151	233	187	060	105	154	115	107	121	330		021	276	263	345	269	257	293	282	046		272				295							
7	Mode	10	10	10	4	10	2	2	2	1	3	2	1	2	1	1	1	1	1	2	2	2	1	1	1	1	1	1	1	1	1	1	1				
	Direction	262	322	348	306	194	112	323	232	262	285	019	012	215	047	210	315	250	270	240	032	059	252	299	276	255	261	264	256	279	276	315	292				
8	Mode	10	10	9	10	6	2	3	3	3	2	1	1	2	2	1	1		1	1	1	1	1	1	1	1	1	1	1	1	1	1	1	1	1	1	1
	Direction	082	301	325	224	027	198	290	344	201	177	276	249	261	318	121	221		233	231	241	313	269	276	268	250	276	271	260	272	277	273	293	269		268	272
9	Mode	9	10	10	6	10	4	4	2	1	1	1	2	1	1	1		1	1	1	1	1	1	1	1	1	1	1			1	1					
	Direction	317	146	296	276	265	245	275	271	117	194	113	214	343	248	225		005	274	265	265	267	255	280	001	275	241	271			257	271					
10	Mode	10	10	10	10	10	3	5	3	2	2	1	2	1	1	1	1	1		1			1	1	1	1					1			1			
	Direction	266	260	327	291	358	002	345	051	286	327	321	346	336	331	062	056	227		255			310	282	141	113					010			094			
11	Mode	10	10	10	10	3	2	3	2	3	2		2	2	1		1	1		1	1	1			1	1	1	1	1	1		1		1		1	1	1
	Direction	059	340	334	336	192	342	038	307	355	328		316	010	057		032	053		054	020	001			307	308	320	338	054	037		324	170		018	271	097
12	Mode	10	10	10	4	2	4	2	3	3	2	1	1	2	1	1	1		1	1	1	1	1			1			1		1	1		1			
	Direction	270	357	358	299	277	049	350	270	011	322	003	278	006	054	024	108		031	065	065	000	147			310			007		274	339		239			
13	Mode	10	6	7	5	4	3	4	1	2	1	1	1	1	1	1	1		1	1		1	1		1	1	1				1						
	Direction	269	025	075	035	349	038	025	358	041	013	298	036	030	008	017	006		041	030		053	002		002	007	008				005						
14	Mode	10	6	9	7	3	1	1	1	1	2	1	1	1	1	11	1	1	1	1	1			1										1			
	Direction	036	286	180	032	109	015	051	042	120	315	166	204	319	220	190	245	273	285	023	042			278										077			
15	Mode	10	10	10	1	5	2	2	3	6	2	1	1	1	1	2	1	1	1	1	1	1	1	1	1	1		1		1							
	Direction	301	269	032	354	354	206	047	269	224	004	322	260	279	004	035	198	349	245	087	034	031	055	060	186	353		300		020							

falling above mode 10 are included as mode 10. All other modal indexes refer to the nearest modal line. The solutions were also tested against the 14 December dispersion curves. Complete modal agreement was found except at 4.9 cph in series 8. Here, the 1 December curves indicate third mode and 14 December curves indicate second mode but at a 2nd-3rd mode resonant region.

Although high modes frequently occur at the low frequencies, the first mode predominates in the high frequency range. This feature is probably caused by the wave guide narrowing with increasing frequency - thus subjecting the higher modes to greater shear until they eventually become unstable. In general, it is felt that the modal solutions are quite good. Notice the good agreement between the wave number solutions and the theoretical modal lines in Figure 9. Credence to this belief is also given by the good fit obtained in the slowness plots of the next chapter. It must be remembered however that any particular modal solution, and especially those with large wave numbers, may have been shifted relative to the dispersion curves by the Doppler effect discussed above. Table IV lists the number of solutions in each mode.

TABLE IV

Number of Acceptable Solutions in Each Mode

Mode	Number of Solutions	Percent of Solutions
1	257	66
2	47	12
3	23	6
4	11	3
5	9	2
6	5	1
7	2	1/2
8	2	1/2
9	5	1
10	31	8
Total	392	100%

Numerous wave solutions which appear to be stationary over several days may be found by referring to Table III. For example the solutions for $f_c = 2.44$ cph show a 2nd mode internal wave traveling $153 \pm 1^\circ$ during series 1, 2, and 3. Similarly, for $f_c = 7.71$, the solutions for series 5, 6, 7, 8, and 9 show $\theta = 265 \pm 15^\circ$ and for $f_c = 8.06$, $\theta = 279 \pm 3^\circ$ during series 8, 9, and 10.

To define the general shape of the energy spectrum, the 45 spectra (three for each series) were ensemble

averaged. Considering that the three spectra from each series are not independent, and allowing for the overlapping in time of several of the series, the resulting spectral estimates have 194 degrees of freedom. For 194 degrees of freedom there is 80% confidence that $.87\sigma^2 < s^2 < 1.13\sigma^2$ and 95% confidence that $.81\sigma^2 < s^2 < 1.21\sigma^2$. A log-log plot of the average spectrum is shown in Figure 15.

The spectrum has been broken into characteristic regions according to slope. The slope of the curve and the power of frequency at which the spectrum falls are identical. Initially (.2 cph to 1.7 cph) where the wave guide ($\omega < N(z)$) occupies the entire water column, the spectrum falls as $f^{-2.2}$. At 1.7 cph, the slope changes to f^{-1} and the wave guide begins to narrow with succeeding spectral estimates (i.e., for f_c = 1.74 cph, $\Delta z = 4000_m$, for f_c = 2.09 cph, $\Delta z = 1430_m$, and for f_c = 2.44 cph. $\Delta z = 860_m$; where Δz is the thickness of the wave guide). From 5 cph to 12 cph, the spectrum falls as $f^{-3.25}$. Above 12 cph, no internal waves appear to be present (the 4 acceptable solutions above 12 cph in Table III have been Doppler shifted), and the rate of fall of the spectrum begins to decrease until at 50 cph it reaches the inherent noise level of measurement. This region of zero slope indicates a root mean square noise amplitude, ζ rms (h_c), of .014 meters.

The height of the peak at 4.2 cph lies between the 80% and 95% confidence limits. Also, the individual series

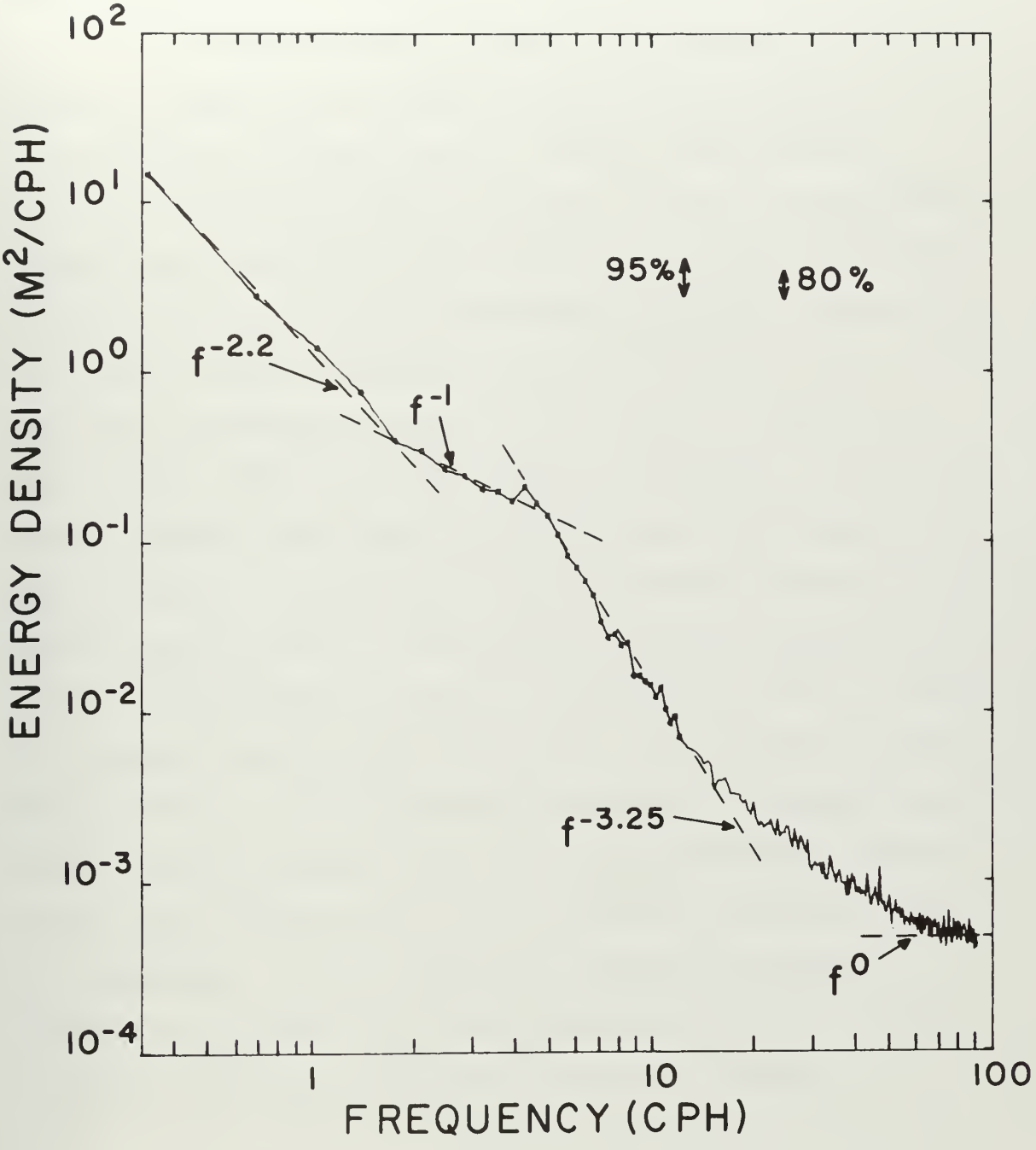

Figure 15. Average energy spectrum.

solutions for this frequency do not indicate any apparent reason for the peak's existence. Therefore, it is felt that the peak has no statistical significance.

The region between 1.7 and 5 cph coincides with the region of good wave solutions and the energy appears to be attributable to internal waves. Using a Richardson's number instability argument, Phillips (1966) has proposed a theoretical equilibrium spectrum for first mode propagation within the thermocline for frequencies such that the stability layer is small compared to the total depth. His spectrum is proportional to f^{-1} for $kd \ll 1$ and to f^{-3} for $kd \gg 1$ (where d is the thermocline depth). Since preceding analysis has shown many solutions of mode higher than one within the region $kd \ll 1$, the agreement between the observed spectrum and the equilibrium spectrum indicates that the f^{-1} power law may apply in general for $kd \ll 1$, and is not limited solely to the first mode. The change in slope from f^{-1} to $f^{-3.25}$ occurs where there is a rapid narrowing of the wave guide, and, as Phillips predicted, where $kd \cong 1$ (see Figures 6 and 7). For $kd \gg 1$, the first mode is predominant and the agreement between the observed spectrum ($f^{-3.25}$) and the equilibrium spectrum (f^{-3}) furnishes additional support to Phillips' Theory.

CHAPTER VI

DIRECTIONAL PROPAGATION AND POSSIBLE SOURCES

To determine whether there were any preferred directions of propagation, the accepted solutions (Table III) were subjected to further analysis. Each solution was spread out over its beam width and normalized so that

$$\int_0^{360^\circ} S(\psi)\, d\psi = 1 \qquad (15)$$

where $S(\psi) = 1/\Delta\theta \; ; \; \theta - \Delta\theta/2 \le \psi \le \theta + \Delta\theta/2$

$S(\psi) = 0 \; ; \; \psi < \theta - \Delta\theta/2, \; \psi > \theta + \Delta\theta/2$

The solutions were then quantized in one degree intervals and added together.

$$P(j) = \sum_i S_i(j) \; ; \; j = 1/2, \; 3/2, \ldots 719/2 \qquad (16)$$

where i indexes the solutions and j represents the mid-direction of the interval. Finally a 10 degree wide running mean filter was used to smooth the results.

$$Q(\ell) = \sum_{m=\ell-\frac{9}{2}}^{\ell+\frac{9}{2}} P(m), \; \ell = 1, 2 \ldots 360 \; ; \; P(-n) = P(360-n) \qquad (17)$$

The resulting beam patterns are shown in Figure 16. The top pattern includes all fifteen series. The remaining 5 patterns include three series each and show the changes which occur with time. Several strong lobes are noticeable

SERIES 1-15

SERIES 1-3

SERIES 4-6

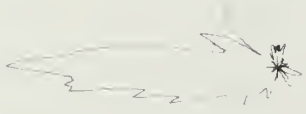

SERIES 7-9

SERIES 10-12

SERIES 13-15

Figure 16. Horizontal beam patterns.

within the patterns. The prominent lobe toward 270° provides an interesting example. It is virtually absent during the first 3 series. It begins to appear during the next 3 series, and for series 7 to 9, overshadows any other direction. It then decreases but remains present for the final 6 series. The existence of these lobes leads to the conclusion that preferential directions indeed do exist.

The existence of directional propagation leads, in turn, to the consideration of possible sources. Azimuthal information is provided by the beam patterns. To determine range, the dispersive character of the wave propagation is utilized. The wave energy travels at the group velocity,

$$G_n(f)=\frac{\partial\omega}{\partial k}=\frac{\partial f}{\partial\lambda_n^{-1}}$$ (where n indexes the mode)

which is the slope of the local tangent to the dispersion curves at $(f, 1/\lambda_n)$. If the source is localized, so that the distance of travel is the same for all wave groups, then for two wave groups arriving at t and t + Δ t:

$$X=G(f_0)\,t \tag{18}$$

$$X=G(f_1)\,(t+\Delta t) \tag{19}$$

so that

$$XG^{-1}(f_0)=t \tag{20}$$

$$XG^{-1}(f_1)=t+\Delta t \tag{21}$$

Letting $\Delta G^{-1}=G^{-1}(f_1)-G^{-1}(f_0)$ and subtracting equation (20) from equation (21)

$$X=\Delta t/\Delta G^{-1} \tag{22}$$

Thus, range to a source is obtained by making slowness plots (time of arrival vs. inverse group velocity). The slope and t-intercept of a reasonable straight line fit give range and time of generation respectively. The slowness plots for the lobes centered at 270°, 070° and 025° are shown in Figures 17, 18 and 19. The slope for 270° ($\cong$ 1.59 day-meters/sec gives a distance of approximately 75 miles. Looking in the reciprocal direction (i.e., 090°) at a distance of 75 miles from FLIP's track, one observes a prominent ridge of seamounts (labeled "A" in Figure 3).

In Figure 18 several different slopes are apparent. The steepest slope (7.14 day-meters/sec) indicates a distance of 330 miles and again, the source seems to be a cluster of seamounts (labeled "B" in Figure 3). The next steepest slope (2.18 day-meters/sec) indicates a distance of 100 miles and the seamount marked "C" in Figure 3 seems to be the source. The least slope (.92 day-meter/sec) indicates a distance of 43 miles. Since this solution occurs during the time when FLIP was rapidly drifting toward the south, it is felt that the seamount at "D" (Figure 3) was the source and that the wave group also was subjected to advection in a southerly direction.

In Figure 19, only the slope of the heavy line (5.00 day-meters/sec) corresponds to a topographic feature (range = 233 miles - area labeled "E" in Figure 4). The other lines give ranges of 110, 345, and 24 miles. They are

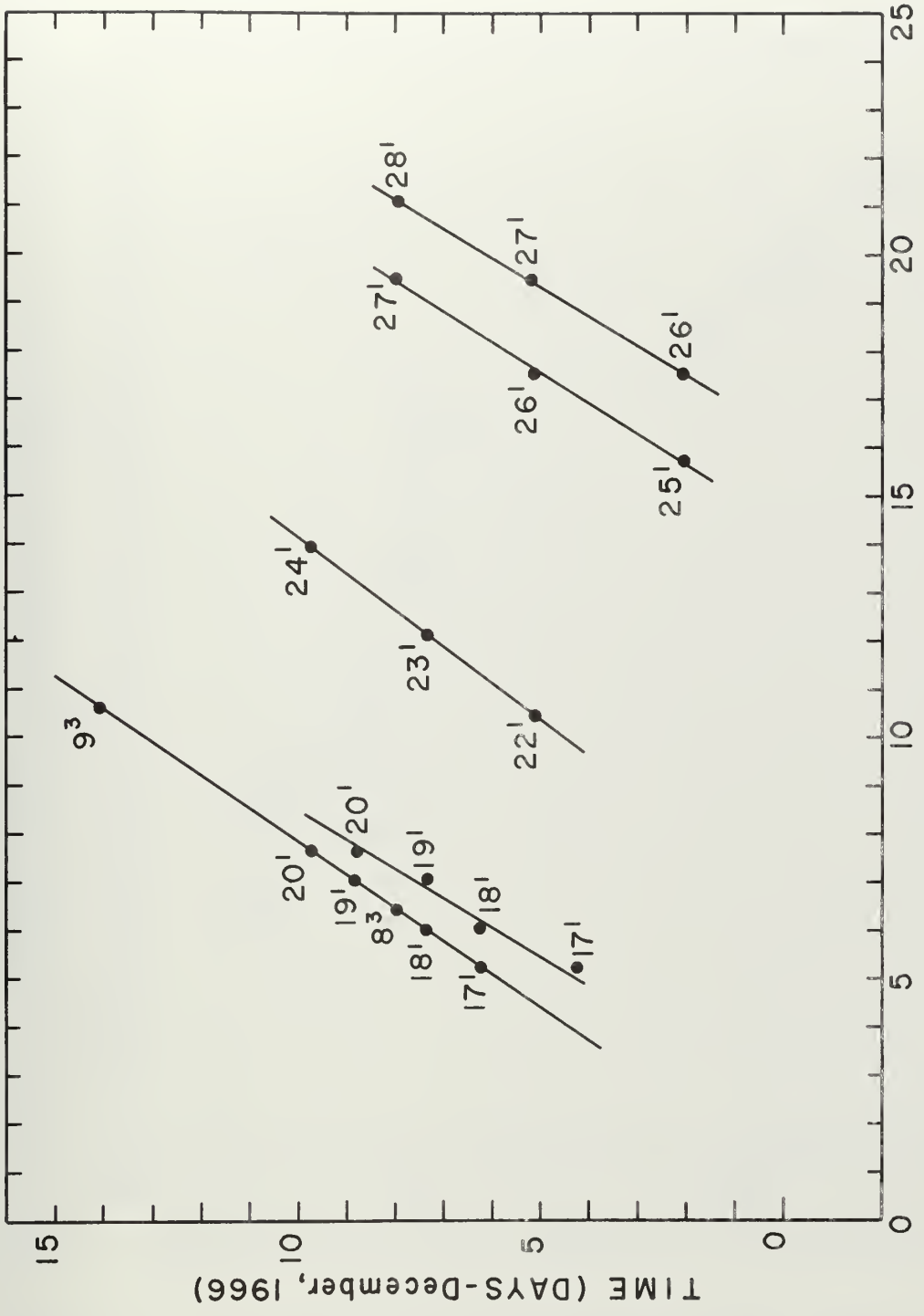

Figure 17. Slowness plot for direction 270°. Numbers refer to frequency band numbers of Table III. Superscripts indicate mode.

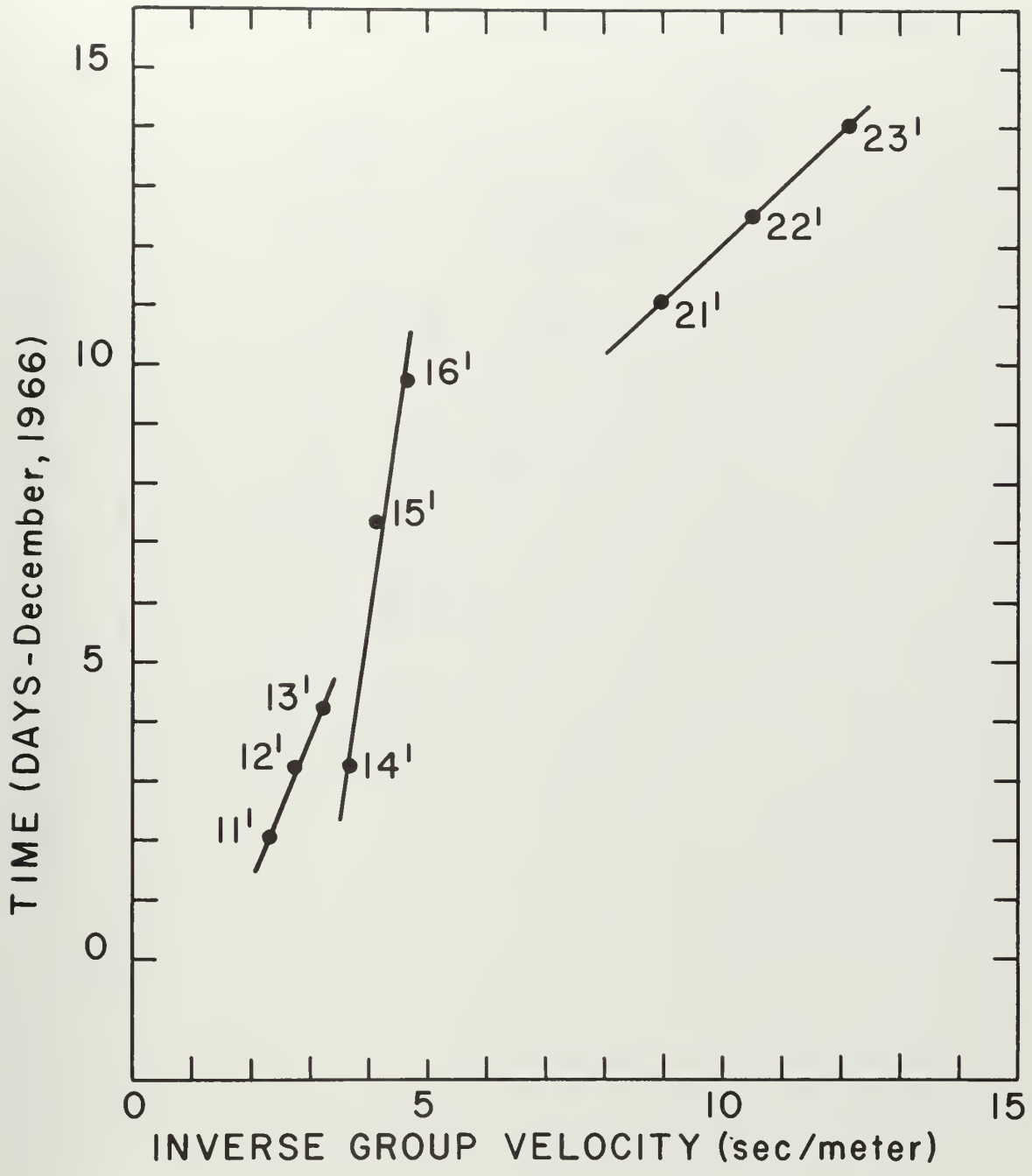

Figure 18. Slowness plot for direction 070°. Numbers refer to frequency band numbers of Table III. Superscripts indicate mode.

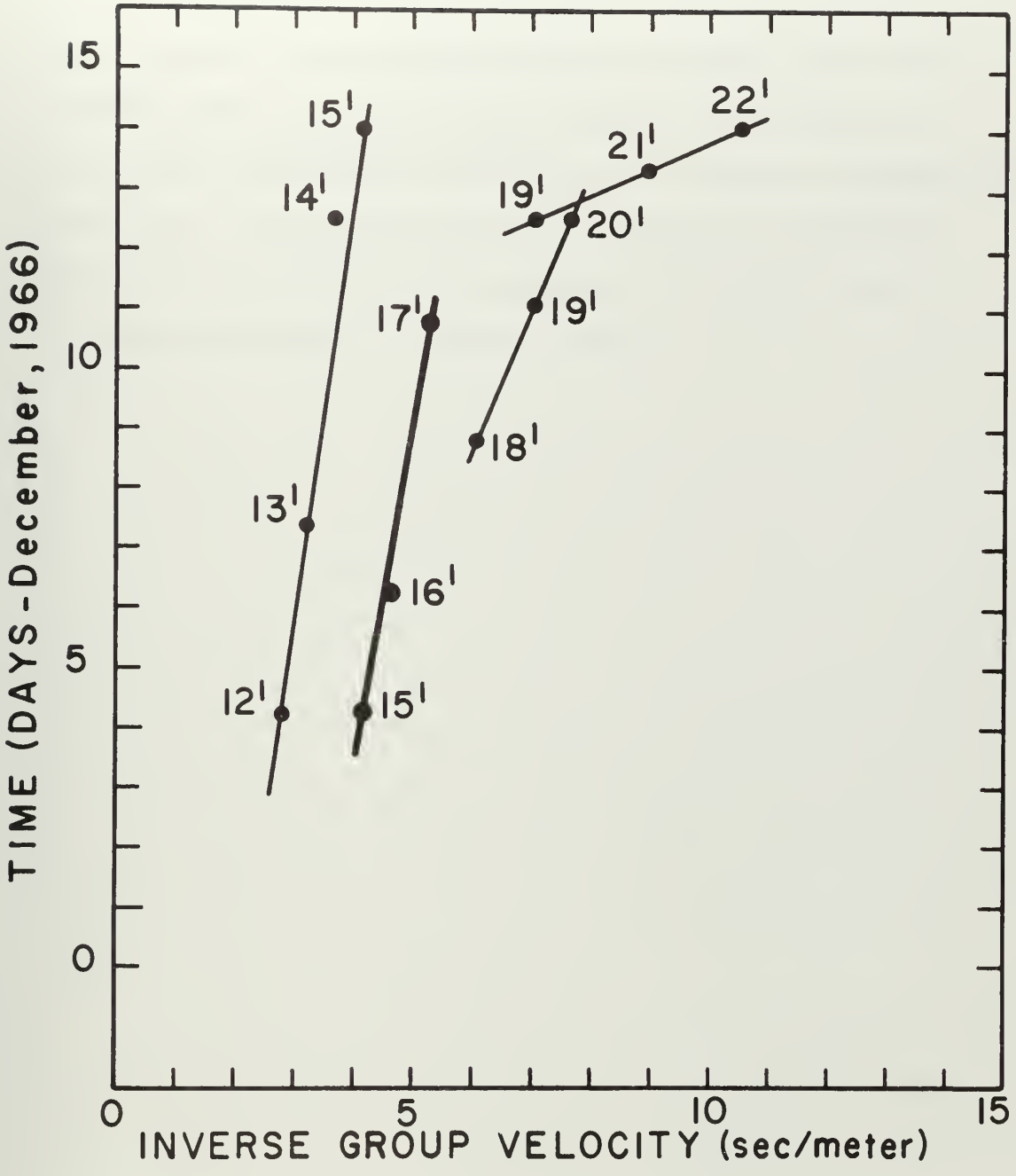

Figure 19. Slowness plot for direction 025°. Numbers refer to frequency band numbers of Table III. Superscripts indicate mode.

shown to indicate that many of the straight line fits give ranges to which no correlation with topography was found.

The quantity of solutions used to determine the slopes makesthe range determinations subject to doubt. These results were presented not as absolute proof that seamounts act as internal wave sources, but merely to demonstrate that the solutions point to them as likely possibilities. This conclusion is supported by Sandstrom (1966) who has shown that topographic features tend to increase the energy in internal waves.

CHAPTER VII

CONCLUSIONS

High frequency internal waves in the deep ocean are characterized as a broad band phenomenon with a continuous distribution in frequency. The spectral shape is consistent with Phillips' theory of a shear limiting process, and the predominance of the first mode at high frequency gives additional emphasis to the importance of shear instability in internal wave propagation.

Over short intervals of time, a narrow frequency band within the continuum displays great simplicity in modal and directional structure and can be adequately described as a horizontally plane wave (i.e., small beam width) of a single vertical mode. In addition, it has been shown that this simplified structure is statistically stationary for time-spans on the order of several days. This structural simplicity indicates that the waves are well dispersed and implies the existence of fairly localized (both in time and space) sources.

Considering the properties of the total (broad band) wave field, additional evidence of localized sources is found. The horizontal nature of the wave field displays definite anisotropy, indicating well-defined directions of narrow-beamed wave propagation. While the exact character

of the anisotropy may change appreciably in times of the order of several days, well defined directions of narrow-beamed propagation always appear to be present.

The time-history of the wave field displays the presence of dispersive wave trains. As well as indicating localized sources, their presence makes possible the calculation of source range. These range determinations, coupled with the well-defined propagation directions, indicate that nearby topographic features such as seamounts act as generators of high frequency internal waves.

In view of the wide distribution of seamounts throughout the oceanic basin, the superposition of arrivals from the multitude of sources should produce a confused "internal sea". Therefore, the waves must not persist over long propagation paths.

LIST OF REFERENCES

Charnock, H. (1965). Preliminary Study of the Directional Spectrum of Short Period Internal Waves. Proc. 2nd U.S. Navy Symp. Mil. Oceanog., pp. 175-178

Cooley, J.W. and Tukey, J.W. (1965). An Algorithm for the Machine Calculation of Complex Fourier Series. Math. Comp., V. 19, pp. 279-301.

Cox, C.S. (1962). Internal Waves. Part 2. The Sea. (Ed. M.N. Hill). Vol. I, pp. 752-763. New York: Interscience.

Eckart, C. (1960). Hydrodynamics of Oceans and Atmospheres. Oxford: Pergamon Press.

Eckart, C. (1961). Internal Waves in the Ocean. The Physics of Fluids. Vol. 4, 7, pp. 791-799.

Fisher, F.H. and Spiess, F.N. (1963). FLIP - Floating Instrument Platform. J. Acoust. Soc. Amer., 35. pp. 1633-1644.

Fjeldstad, J.E. (1933). Interne Wellen. Geophys. Publ. Vol. 10, 6, pp. 1-35.

Good, D.E. (1968). Isotherm Followers for Ocean Research. Proc. Annual I.S.A. Symp. In preparation.

Greenhill, (1887). Wave Motion in Hydrodynamics. Amer. J. Math. 9.

Harris, B., Ed. (1966) Spectral Analysis of Time Series. New York: Wiley.

Haubrich, R.A. (1965). Earth Noise, 5 to 500 Millicycles per Second. Part 1. J. Geophys. Res., Vol. 70, 6, pp. 1415-1427.

LaFond, E.C. (1961a). The Isotherm Follower. J. Marine Res., Vol. 19, I, pp. 33-39.

LaFond, E.C. (1961b). Boundary Effects on the Shape of Internal Waves. Indian Jour. of Meteorology and Geophys.

LaFond, E.C. (1962a). Internal Waves. Part 1. The Sea. (Ed. M. N. Hill). Vol. I, pp. 731-751.

LaFond, E.C. (1962b). Internal Waves and Their Measurement. Marine Sciences Instrumentation. Vol. 1. New York: Plenum Press.

LaFond, E.C. (1964). Three-dimensional Measurements of Sea Temperature Structure. Studies on Oceanography.

Menard, H.W. (1960). Unpublished Chart.

Metcalf, W.G., Voorhis, A.S., and Stalcup, M.C. (1962). The Atlantic Equatorial Undercurrent. J. Geophys. Res., Vol. 67, 6, pp. 2499-2508.

Phillips, O.M. (1966). The Dynamics of the Upper Ocean. Cambridge: University Press.

Sandstrom, H. (1966). The Importance of Topography in Generation and Propagation of Internal Waves. Ph.D. Thesis, University of California, San Diego.

Squier, E.D. (1967). A Variable Frequency Thermometer. Marine Physical Laboratory Technical Memoranda, 183.

Stokes, G. (1847). On the Theory of Oscillatory Waves. Camb. Trans., VIII, paper I, p. 212.

Tolstoy, I. (1963). The Theory of Waves in Stratified Fluids Including the Effects of Gravity and Rotation. Reviews of Modern Physics, Vol. 35, 1, pp. 207-30.

Ufford, C.W. (1947). Internal Waves Measured at Three Stations. Trans. Amer. Geophys. Union. Vol. 28, 1, pp. 87-95.

Webb, (1882) Math. Tripos Papers.

APPENDIX A

Theory of Small Amplitude Internal Waves

I. List of Symbols

c	velocity of sound
f	inertial frequency
g	acceleration of gravity
k	wave number magnitude
k_x	x-component of wave number vector
k_y	y-component of wave number vector
n	mode index
t	time
x	horizontal coordinate
y	horizontal coordinate orthogonal to x
z	vertical coordinate (positive up)
D	depth of bottom
F	force
N	stability frequency
α	specific volume
ζ	vertical displacement
ρ	density
ω	angular frequency
dV	infinitesimal volume
Δz	small vertical displacement
$(\ddot{\ })$	second derivative with respect to time
$(\ )_{zz}$	second derivative with respect to Z

II. Infinitesimal Waves

The following presentation consists of only those aspects of internal wave theory necessary to the understanding of the observational and analytical techniques employed in this dissertation. More detailed formulations may be found in Eckart (1960) and Tolstoy (1963).

Consider a vertically stratified, compressible fluid at rest in a gravity field. If a parcel of fluid is raised vertically from its equilibrium position and then released, it will tend to sink with the force:

$$F = g\left(\rho - \left(\rho + \frac{\partial \rho}{\partial z}\Delta z\right) dV\right) - \rho \frac{g^2}{c^2} \Delta z\, dV \qquad (1A)$$

the first term being due to buoyancy and the second compressibility. The vertical equation of motion becomes:

$$\rho dV \ddot{z} = -g \frac{\partial \rho}{\partial z} z dV - \rho \frac{g^2}{c^2} z dV \qquad (2A)$$

For infinitesimal motions, the solution to equation (2) is that of a harmonic oscillator with the frequency:

$$N(z) = \sqrt{-\frac{g}{\rho}\frac{\partial \rho}{\partial z} - \rho \frac{g^2}{c^2}} \qquad (3A)$$

Equation (3A) defines the Brunt-Vaisala or stability frequency. In the upper ocean, the compressibility term is generally small compared to the buoyancy term and is usually neglected. Thus we have harmonic motion caused by buoyancy forces due to density stratification.

Starting with the three-dimensional equations of motion, mass conservation, and invoking the following assumptions:

1) N = N(z) and is independent of horizontal coordinates

2) Mean velocities are equal to zero

3) Boussenesq Approximation - Density variation may be neglected except where it causes buoyant forces

4) Nonlinear terms are negligible

we arrive at the first order equation of motion

$$\zeta_{zz} - \frac{N^2(z)-\omega^2}{\omega^2-f^2}\,\nabla_H \zeta = 0 \qquad (4A)$$

where ω is the angular frequency and f is the inertial frequency due to rotation of the earth and ζ is the vertical displacement from equilibrium.

If we assume a solution of plane horizontally progressive waves of the form

$$\zeta(x,y,z,t) = \zeta(z)\, e^{i(k_x x + k_y y - \omega t)} \qquad (5A)$$

$$\text{and } k^2 = k_x^2 + k_y^2$$

then (4A) becomes

$$\zeta_{zz} + \frac{N^2-\omega^2}{\omega^2-f^2}\, k^2 \zeta = 0 \qquad (6A)$$

Internal waves have their maximum amplitude below the surface of the water column and at this maximum

$$\zeta_{zz} < 0$$

but $$\frac{\zeta_{zz}}{\zeta} = -k^2 \frac{N^2 - \omega^2}{\omega^2 - f^2}$$

Therefore either $f^2 < \omega^2 < N^2$ or $N^2 < \omega^2 < f^2$. In the ocean $N^2 \gg f^2$ so that the former condition is the correct one, and f and N_{max} are the lowest and highest frequencies permitted to free internal waves of form (5A).

If $\omega^2 \gg f^2$ then equation (6A) becomes

$$\zeta_{zz} + k^2 \frac{N^2 - \omega^2}{\omega^2} \zeta = 0 \qquad (7A)$$

The boundary conditions for our purposes are

$\zeta = 0$ at $z = 0$ surface

$\zeta = 0$ at $z = -D$ bottom

The free surface boundary condition may be used at the surface but has very little effect on the internal modes.

For arbitrary N(z) and fixed ω, solutions to equation (7A) are found by iterative numerical techniques - starting with $\zeta = 0$ at $z = -D$ and working to satisfy the surface boundary condition. For a given ω, solutions can be found for an infinite number of discrete values of K. For each such value of K_n, there is a corresponding amplitude function ζ_n. The index n relates to the number of amplitude maxima within the water column, and (n-1) to the number of nodes or zero crossings between the maxima.

Solutions will be progressive if $\omega < N(z)$ somewhere in

the water column. $\zeta_n(z)$ will be "trigonometric" where $\omega<N(z)$ and "exponential" where $\omega>N(z)$ (see Figure 1A).

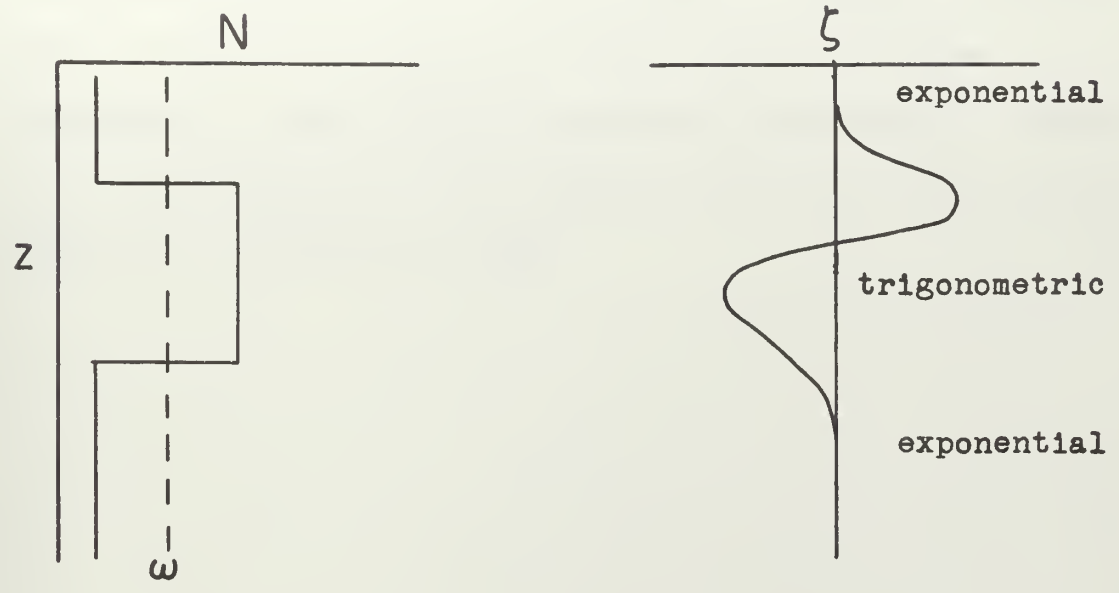

Figure 1A. 2nd Mode Amplitude Function

Within the thermocline where the density gradient, and therefore N(z), is a maximum, the appropriate variation of physical parameters and their effects on specific volume are given in Table IA

TABLE IA

The Variations of Physical Parameters in the thermocline and their effects on specific volume

Parameter	Variation	X $\frac{1}{\alpha}\frac{\partial \alpha}{\partial(\ )}$	Specific Volume Change
Temperature	$-8^{\circ}C$	$-2X10^{-4}/^{\circ}C$	$-1.6X10^{-3}$
Salinity	+.3 ‰	$-8X10^{-4}/‰$	$-2.4X10^{-4}$
Pressure	+100db	$-4X10^{-4}/100db$	$-4X10^{-4}$

It has already been shown that internal waves are oscillations of isodensity surfaces. Since temperature is the dominant parameter within the thermocline, the motions of an isodensity surface may be approximated by those of an isotherm. This approximation is very convenient since temperature is much easier to measure than density. Temperature measurements for this reason have been widely used for obtaining observational data.

APPENDIX B

Interpolation Scheme

The following parameters were sequentially sampled from each sea-sensing unit:

$$D_a,\ T_1,\ T_2,\ T_3,\ T_4,\ D_b$$

where D = depth and T = temperature.

Then the depth D_i of each thermometer when sampled may be found to first order by

$$\Delta D_i = \frac{(D_b - D_a)}{5} i,\ i = 1,4$$

$$D_i = D_a + \Delta D_i + \delta_i \tag{12}$$

where δ_i is the vertical offset of the i^{th} thermometer from the servo-system thermistor.

The depth of the isotherm (D_T) to first order is then found by using the two temperature measurements which bracket the isotherm:

$$D_T = D_i + \left[(D_{i+1} - D_i)/(T_i - T_{i+1}) \right] (T_i - T)$$

where T is the temperature of the desired isotherm.

APPENDIX C

Doppler Effect

Phase velocity, c, is defined as

$$c = \omega/k = f/\lambda^{-1}$$

When sampling at three points simultaneously, the Doppler shift occurs only in frequency, leaving the wavelength unaffected. Thus:

$$c + \Delta c = \frac{\omega + \Delta\omega}{k} = \frac{f + \Delta f}{\lambda^{-1}}$$

$$\Delta c = \Delta f/\lambda^{-1}$$

For frequency 9.47 cph of series 8, $\lambda^{-1} = 8.62 \times 10^{-3}\, m^{-1}$. $\lambda^{-1} = 8.62 \times 10^{-3} m^{-1}$ occurs at 7.90 cph on the first modal curve of Figure 6.

$$\Delta c = \frac{9.47 - 7.90}{8.62 \times 10^{-3}} \times \frac{10^2}{3600} = \frac{1.57}{.31} \cong 5 \frac{cm}{sec}$$